Theoretical estimates of sulfoxyanion triple-oxygen equilibrium isotope effects and their implications

Jordon D. Hemingway[a,b,1], Madison L. Goldberg[b], Kevin M. Sutherland[b], David T. Johnston[b]

[a]*Geological Institute, Department of Earth Sciences, ETH Zürich, Zürich, Switzerland*
[b]*Department of Earth and Planetary Sciences, Harvard University, Cambridge, MA, USA*

Abstract

Triple-oxygen isotope ($\delta^{18}O$ and $\Delta'^{17}O$) analysis of sulfate is becoming a common tool to assess several biotic and abiotic sulfur-cycle processes, both today and in the geologic past. Multi-step sulfur redox reactions often involve intermediate sulfoxyanions such as sulfite, sulfoxylate, and thiosulfate, which can rapidly exchange oxygen atoms with surrounding water. Process-based reconstructions therefore require knowledge of equilibrium oxygen-isotope fractionation factors ($^{18}\alpha$ and $^{17}\alpha$) between water and each individual sulfoxyanion. Despite this importance, there currently exist only limited experimental $^{18}\alpha$ data and no $^{17}\alpha$ estimates due to the difficulty of isolating and analyzing short-lived intermediate species. To address this, we theoretically estimate $^{18}\alpha$ and $^{17}\alpha$ for a suite of sulfoxyanions—including several sulfate, sulfite, sulfoxylate, and thiosulfate isomers—using quantum computational chemistry. We determine fractionation factors for sulfoxyanion "water droplets" using the B3LYP/6-31G+(d,p) method; we additionally determine higher-order method (CCSD/aug-cc-pVTZ and MP2/aug-cc-pVTZ) and anharmonic zero-point energy (ZPE) scaling factors using a suite of gaseous sulfoxy compounds and test their impact on resulting sulfoxyanion fractionation-factor estimates. When including redox state-specific CCSD/aug-cc-pVTZ and anharmonic ZPE scaling factors, our theoretical $^{18}\alpha$ predictions for protonated isomers closely agree with all existing experimental data, yielding root-mean-square errors of 1.8 ‰ for $SO_3(OH)^-/H_2O$ equilibrium (n = 18 experimental conditions), 2.2 ‰ for $SO_2(OH)^-/H_2O$ (n = 27), and 3.9 ‰ for $S_2O_2(OH)^-/H_2O$ (n = 3). This result supports the idea that oxygen exchange occurs via isomers containing oxygen-bound protons. By combining $^{18}\alpha$ and $^{17}\alpha$ predictions, we additionally estimate that $SO_3(OH)^-$, $SO_2(OH)^-$, $SO(OH)^-$, and $S_2O_2(OH)^-$ exhibit $\Delta'^{17}O$ values as much as 0.167 ‰, 0.097 ‰, 0.049 ‰, and 0.153 ‰ more negative than equilibrated water at Earth-surface temperatures (reference line slope = 0.5305). This theoretical framework provides a foundation to interpret experimental and observational triple-oxygen isotope results of several sulfur-cycle processes including pyrite oxidation, microbial metabolisms (e.g., sulfate reduction, thiosulfate disproportionation), and hydrothermal anhydrite precipitation. We highlight this with several examples.

Keywords: computational predictions; microbial sulfate reduction; pyrite oxidation; sulfate; triple-oxygen isotopes

*Corresponding author; email: jordon.hemingway@erdw.ethz.ch

1. Introduction

Sulfur can exist in a range of redox states from S(-II) to S(+VI). As such, its oxidation and reduction represent major electron fluxes into and out of Earth's biosphere; these fluxes regulate atmospheric O_2 content and the Earth-surface redox state over multi-million year timescales (Berner, 2001). Today, dissolved marine sulfate [S(+VI) redox state] constitutes one of the largest oxidant reservoirs on Earth's surface (Blättler et al., 2018), whereas sulfide minerals such as pyrite [FeS_2; S(-I)] contained in marine sediments and sedimentary rocks constitute one of the largest reductant reservoirs (Berner, 1984).

Several biotic and abiotic processes can transfer sulfur between these oxidized and reduced forms, often via sulfoxyanion species that exist at intermediate redox states. For example, microbial sulfate reduction (MSR) is a metabolism that gains energy in the absence of O_2 by reducing dissolved sulfate to hydrogen sulfide [S(-II)]—the precursor to pyrite—via the intermediate species sulfite [S(+IV)] (Fike et al., 2015). Related metabolisms gain energy by simultaneously oxidizing and reducing sulfur to sulfate and sulfide via the disproportionation of intermediate redox compounds such as sulfite, zero-valent sulfur [S(0)], or the mixed-valence species thiosulfate [S(-I)/S(+V); see Vairavamurthy et al. (1993) for atom-specific redox state determination] (Jørgensen, 1990; Fike et al., 2015). Similarly, the (a)biotic oxidative weathering of pyrite in exhumed rocks must occur via sulfite and thiosulfate intermediates, although the exact mechanism is complex and not fully constrained (e.g., Balci et al., 2007; Schoonen et al., 2010; Kohl and Bao, 2011). Furthermore, sulfoxyanion species existing in intermediate redox states are generally short-lived at Earth-surface conditions. For example, the hydrolysis and oxidation of sulfur dioxide gas [S(+IV)] to sulfate in atmospheric water—which represents a major pathway of acid rain formation—occurs on the order of microseconds (Brandt and van Eldik, 1995). The residence time of intracellular sulfite produced during MSR is similarly estimated to be on the order of microseconds before it is either fully reduced to hydrogen sulfide or reoxidized to sulfate (Bertran et al., 2020). Thus, even though the overall abundance of intermediate sulfoxyanions on Earth's surface at any point in time is low, nearly all sulfur-cycle processes require their transient production and consumption (e.g., Jørgensen, 1990).

One method to assess the relative importance of various sulfur-cycle processes is by analyzing the sulfur and oxygen isotope compositions of sulfate ($^{33}S/^{32}S$, $^{34}S/^{32}S$, $^{36}S/^{32}S$, $^{17}O/^{16}O$, and $^{18}O/^{16}O$; here reported as $\Delta^{33}S$, $\delta^{34}S$, $\Delta^{36}S$, $\Delta'^{17}O$, and $\delta^{18}O$, respectively; see Sec. 2.1). For example, Wing and Halevy (2014) and Bertran et al. (2020) showed that ^{34}S and ^{18}O fractionation during MSR represents a balance between kinetic and equilibrium fractionation factors; MSR rates in marine sediments can thus be predicted using the $\delta^{34}S$ and $\delta^{18}O$ values of residual sulfate. Similarly, $\delta^{34}S$, $\delta^{18}O$, and $\Delta'^{17}O$ values of dissolved sulfate in rivers has been used to estimate the relative importance of anaerobic pyrite weathering, aerobic pyrite weathering, and evaporite dissolution on land (e.g., Turchyn et al., 2013; Burke et al., 2018; Killingsworth et al., 2018; Hemingway et al., 2020; Burt et al., 2021; Kemeny et al., 2021). Furthermore, sulfate is preserved in minerals such as gypsum ($CaSO_4$), barite ($BaSO_4$), and carbonate (as carbonate-associated sulfate, or CAS; $CaCO_3 \cdot SO_4$); the sulfur and oxygen isotope compositions of these minerals can thus be

used to reconstruct sulfur-cycle processes through time.

Despite the utility of sulfate isotopes as geologic tracers, their proper interpretation requires knowledge of fractionation factors for each step of each sulfur-cycle process. Specific to $\delta^{18}O$ and $\Delta'^{17}O$, intermediate sulfoxyanions can rapidly exchange oxygen atoms with surrounding water, potentially exhibiting redox state- and isomer-specific equilibrium fractionation factors (e.g., Pryor and Tonellato, 1967; Betts and Voss, 1970; Müller et al., 2013a; Wankel et al., 2014; Goldberg, 2021). Thus, the final oxygen isotope composition of sulfate produced or consumed by any process should depend strongly on (i) the isotope composition of water in which it formed and (ii) the specific intermediate sulfoxyanion species involved. Although some empirical ^{18}O fractionation estimates exist for sulfate, sulfite, and thiosulfate (Lloyd, 1968; Chiba et al., 1981; Müller et al., 2013a; Wankel et al., 2014; Goldberg, 2021), many sulfoxyanion oxygen-isotope fractionation factors—especially those for ^{17}O—remain unknown due to the difficulty of experimentally measuring these short-lived compounds. This lack of fractionation factor constraints hinders our ability to interpret sulfate $\delta^{18}O$ and $\Delta'^{17}O$ values, both today and in the geologic past.

In the absence of experimental constraints, quantum-chemistry computational methods have been shown to yield acceptable triple-oxygen isotope fractionation factor estimates for a range of oxygen-containing anions and minerals (e.g., Cao and Liu, 2011; Hayles et al., 2018; Schauble and Young, 2021; Yeung and Hayles, 2021). Importantly, $\Delta'^{17}O$ estimates are particularly robust since any biases largely cancel due to the mass-dependent nature of equilibrium ^{17}O fractionation (Cao and Liu, 2011). Thus, if computational ^{18}O fractionation factors can be shown to reasonably match experimental constraints, then $\Delta'^{17}O$ is expected to be accurate within analytical uncertainty.

Specific to sulfoxyanions, Eldridge et al. (2016) showed that different protonated isomers can exhibit unique sulfur-isotope fractionation factors; here, we hypothesize the same is true for oxygen isotopes. Additionally, protonated isomers likely control the rate at which oxygen atoms exchange with water. For example, Betts and Voss (1970) and Pryor and Tonellato (1967) showed that sulfite and thiosulfate exchange rates increase exponentially with decreasing pH due to the increasing abundance of isomers containing oxygen-bound protons, which are more reactive than non-protonated isomers. Because of this importance, we seek to computationally estimate triple-oxygen isotope fractionation factors for all major sulfoxyanion isomers. We specifically consider: (i) SO_4^{2-} and $SO_3(OH)^-$ [S(+VI), collectively termed "sulfate"]; (ii) SO_3^{2-}, $(HS)O_3^-$, $SO_2(OH)^-$, and dissolved $SO_{2(aq.)}$ gas [S(+IV), collectively termed "sulfite"]; (iii) SO_2^{2-}, $(HS)O_2^-$, $SO(OH)^-$, (HS)O(OH), and $S(OH)_2$ [S(+II), collectively termed "sulfoxylate"]; and finally (iv) $S_2O_3^{2-}$, $(HS)SO_3^-$, and $S_2O_2(OH)^-$ [mixed valence S(-I)/S(+V), collectively termed "thiosulfate"] (Fig. 1).

The aim of this study is to: (i) outline the necessary notation and quantum mechanical theory to computationally estimate triple-oxygen isotope fractionation factors (Sec. 2); (ii) describe the computational methods used, including those to estimate anharmonic zero-point energy (ZPE) and methodological scaling factors (Sec. 3); (iii) report predicted fractionation factors and compare to available experimental results from the literature (Sec. 4); and finally (iv) interpret these fractionation factors within the context of several sulfur-cycle processes and compare predictions to environmental data (Sec. 5). This work—combined with Eldridge et al. (2016)—yields equilibrium fractionation fac-

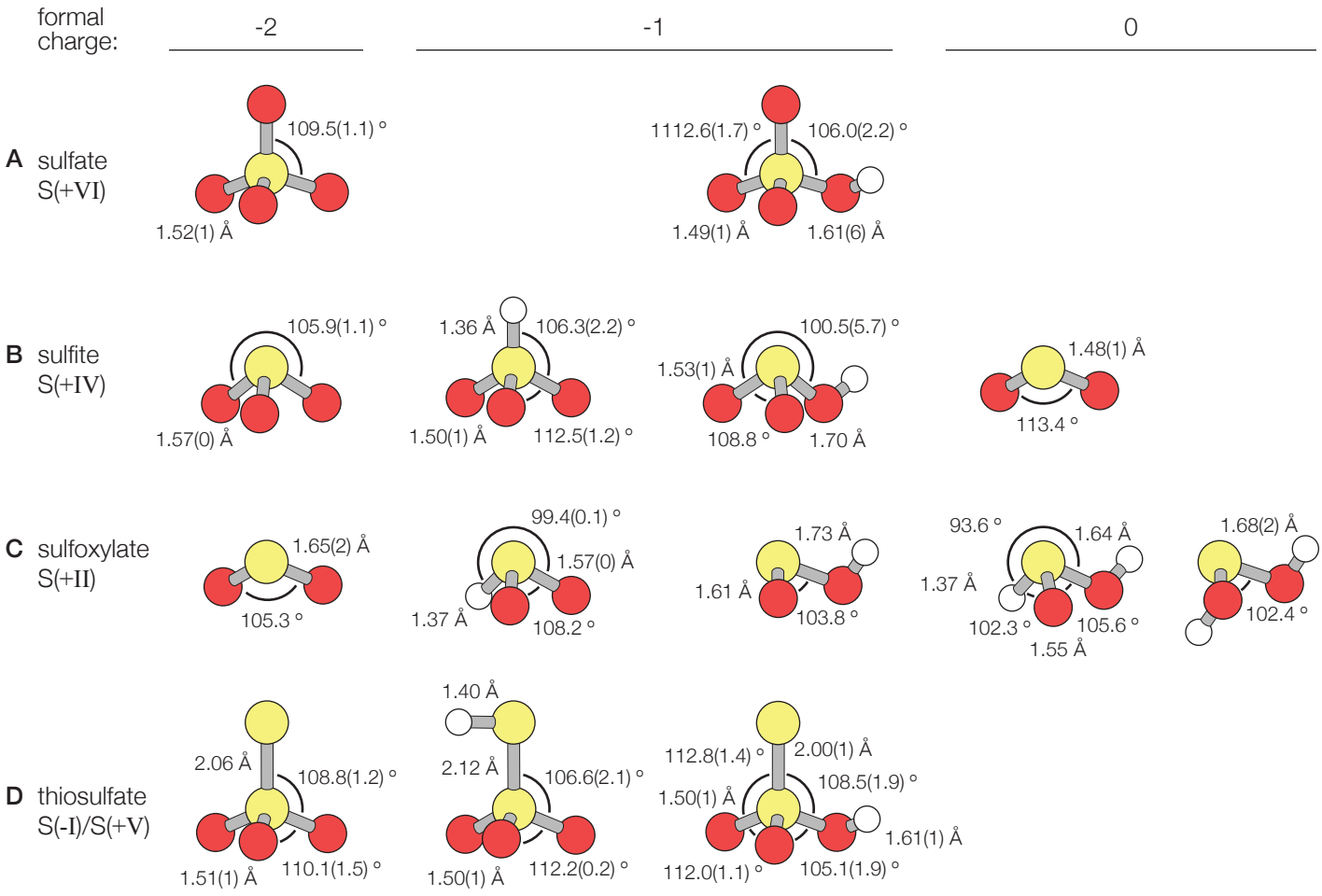

Figure 1: **Ball-and-stick representation of all sulfoxyanion species.** Species are separated by sulfur redox state: (**A**) sulfate species, S(+VI): SO_4^{2-} and $SO_3(OH)^-$; (**B**) sulfite species, S(+IV): SO_3^{2-}, $(HS)O_3^-$, $SO_2(OH)^-$, and $SO_{2(aq.)}$; (**C**) sulfoxylate species, S(+II): SO_2^{2-}, $(HS)O_2^-$, $SO(OH)^-$, (HS)O(OH), and $S(OH)_2$; and (**D**) thiosulfate species, mixed valence [S(-I) sulfanyl and S(+V) sulfonate]: $S_2O_3^{2-}$, $(HS)SO_3^-$, and $S_2O_2(OH)^-$. Reported bond lengths and angles refer to those calculated for a $30 \cdot H_2O$ water droplet cluster using the B3LYP/6-31+G(d,p) method ($-$OH bond lengths and angles are not shown but are included in Table S.3); water molecules are omitted for visual clarity.

tor estimates of all major and minor isotopes ($^{33}S/^{32}S$, $^{34}S/^{32}S$, $^{36}S/^{32}S$, $^{17}O/^{16}O$, and $^{18}O/^{16}O$) for several important sulfoxyanion species.

2. Theory

2.1. Notation

The oxygen-isotope composition of a given compound "A" can be written as

$$\delta^{*}\mathrm{O_A} = \frac{{}^{*}\mathrm{R_A}}{{}^{*}\mathrm{R_{VSMOW}}} - 1, \tag{1}$$

where ${}^{*}\mathrm{R}$ denotes the $^{*}\mathrm{O}/^{16}\mathrm{O}$ ratio, "*" indicates the heavy isotope $^{17}\mathrm{O}$ or $^{18}\mathrm{O}$, and VSMOW is the Vienna Standard Mean Ocean Water international reference standard. Here we report results in units of "permil" by multiplying Eq. 1 by 1000 ‰. For any fractionation process (kinetic or equilibrium), the oxygen-isotope composition of product "A" and reactant "B" are related by the fractionation factor:

$${}^{*}\alpha_{\mathrm{A/B}}(T) = \frac{{}^{*}\mathrm{R_A}}{{}^{*}\mathrm{R_B}}, \tag{2}$$

where we have explicitly added (T) to emphasize that fractionation is temperature-dependent. When considering all three oxygen isotopes, ${}^{18}\alpha_{\mathrm{A/B}}(T)$ and ${}^{17}\alpha_{\mathrm{A/B}}(T)$ are related by the mass law for a given process:

$${}^{17}\theta_{\mathrm{A/B}}(T) = \frac{\ln {}^{17}\alpha_{\mathrm{A/B}}(T)}{\ln {}^{18}\alpha_{\mathrm{A/B}}(T)}. \tag{3}$$

Although each process is described by a unique mass law, fractionation is deemed "mass dependent" if ${}^{17}\theta \approx 1/2$ (i.e., since the mass difference between $^{17}\mathrm{O}$ and $^{16}\mathrm{O}$ is approximately half of that between $^{18}\mathrm{O}$ and $^{16}\mathrm{O}$). To quantify small deviations from the expected mass-dependent $\delta^{17}\mathrm{O}$–$\delta^{18}\mathrm{O}$ relationship, we let

$$\Delta'^{17}\mathrm{O_A} = \ln\left(\delta^{17}\mathrm{O_A} + 1\right) - {}^{17}\theta_{\mathrm{RL}} \ln\left(\delta^{18}\mathrm{O_A} + 1\right), \tag{4}$$

where ${}^{17}\theta_{\mathrm{RL}}$ is the mass law for the "reference line" and prime ($'$) indicates the use of logarithmic $\delta^{*}\mathrm{O}$ values. Like $\delta^{*}\mathrm{O_A}$, here we report $\Delta'^{17}\mathrm{O_A}$ in units of permil by multiplying Eq. 4 by 1000 ‰. Although the choice of reference line is arbitrary, here we set ${}^{17}\theta_{\mathrm{RL}} = 0.5305$ since this corresponds to the high-temperature limit of equilibrium fractionation; i.e., the ratio of reduced masses between isotopes of atomic oxygen (Young et al., 2002). The utility of this limit will become apparent when diagnosing the accuracy of theoretical estimates. Finally, the temperature-dependent $\Delta'^{17}\mathrm{O}$ offset between product "A" and reactant "B" for any fractionation process is defined as

$$\begin{aligned}\Delta\Delta'^{17}\mathrm{O_{A/B}}(T) &= \Delta'^{17}\mathrm{O_A} - \Delta'^{17}\mathrm{O_B} \\ &= \left[{}^{17}\theta_{\mathrm{A/B}}(T) - {}^{17}\theta_{\mathrm{RL}}\right] \ln {}^{18}\alpha_{\mathrm{A/B}}(T).\end{aligned} \tag{5}$$

Our goal is to theoretically estimate ${}^{18}\alpha_{\mathrm{A/H_2O(liq.)}}(T)$ and $\Delta\Delta'^{17}\mathrm{O_{A/H_2O(liq.)}}(T)$ over a range of environmentally relevant temperatures, where "A" is any sulfoxyanion of interest.

2.2. The Bigeleisen-Goeppert Mayer-Urey equation

To estimate fractionation factors, we utilize a modified version of the Bigeleisen-Goeppert Mayer-Urey (B-GM-U) equation, which predicts the equilibrium constant of isotope substitution using translational, rotational, and vibrational reduced partition function ratios (RPFRs) for each isotopically substituted molecule (Bigeleisen and Goeppert Mayer, 1947; Urey, 1947). It is subject to four main approximations: (i) A molecule's rotational motion can be treated as a rigid rotor and (ii) its vibrational motion can be treated as a harmonic oscillator; (iii) the motion of electrons and nuclei are decoupled such that isotopic substitution has no effect on bond strength and molecular structure (the so-called Born-Oppenheimer approximation; Born and Oppenheimer, 1927); and (iv) the ratio of the moments of inertia of two isotopically substituted molecules depends only on their masses and the product of their vibrational frequency ratios (the so-called Teller-Redlich product rule; Redlich, 1935; Wilson et al., 1955).

By following these approximations, utilizing a statistical mechanical treatment of molecular motion, and ignoring multiply substituted isotopologues, the B-GM-U equation can be written as:

$$^{*}\beta_{\mathrm{h}}(T) = \frac{s}{s^{*}} \prod_{i=1}^{3n-x} \left[\frac{u_i^{*}(T)}{u_i(T)}\right]_{\mathrm{TR}} \left[\frac{e^{-u_i^{*}(T)/2}}{e^{-u_i(T)/2}}\right]_{\mathrm{ZPE}} \left[\frac{1-e^{-u_i(T)}}{1-e^{-u_i^{*}(T)}}\right]_{\mathrm{EXC}}, \tag{6}$$

where

$$u_i(T) = \frac{h\omega_i}{k_B T}, \tag{7}$$

h is Planck's constant, ω_i is the harmonic normal mode frequency for degree-of-freedom i, k_B is Boltzmann's constant, T is temperature in Kelvin, s is the rotational symmetry number, n is the number of atoms in the compound of interest, and $x = 5$ for linear molecules or $x = 6$ for nonlinear molecules. As above, "*" denotes terms related to the compound containing the heavy isotope, whereas the subscript "h" indicates the pure harmonic approximation result. We have amended Eq. 6 with the subscripts "TR", "ZPE", and "EXC" to denote contributions from partition functions for translation/rotation, zero-point energy of vibration, and excited vibrational states, respectively.

As defined in Richet et al. (1977), $^{*}\beta$ is the RPFR multiplied by the rotational symmetry number ratio, s/s^{*} (typically, $s/s^{*} = 1$ since isotopic substitution often does not change rotational symmetry). It represents isotope fractionation between the compound of interest and an idealized mono-atomic, non-interacting gas (e.g., an O atom). Oxygen-18 fractionation between two compounds "A" and "B" can thus be written as the ratio of their $^{18}\beta(T)$ values:

$$^{18}\alpha_{\mathrm{A/B}}(T) = \frac{^{18}\beta_{\mathrm{A}}(T)}{^{18}\beta_{\mathrm{B}}(T)}. \tag{8}$$

Following Cao and Liu (2011), we extend this nomenclature for all three oxygen isotopes by defining:

$$^{17}\kappa(T) = \frac{\ln {}^{17}\beta(T)}{\ln {}^{18}\beta(T)}, \tag{9}$$

which similarly represents the equilibrium mass law between the compound of interest and an idealized, mono-atomic,

non-interacting O atom. For any compound of interest, it follows that

$$\lim_{T\to\infty} {}^{17}\kappa(T) = \frac{\left(\frac{1}{^{16}\mathrm{O}} - \frac{1}{^{17}\mathrm{O}}\right)}{\left(\frac{1}{^{16}\mathrm{O}} - \frac{1}{^{18}\mathrm{O}}\right)} = 0.5305, \tag{10}$$

(see Young et al., 2002, for derivation). That is, ${}^{17}\kappa(T)$ should approach the high-temperature limit of equilibrium fractionation. Combining Eqs. 3, 8, and 9, the mass law for equilibrium fractionation between two compounds "A" and "B" can be written as a function of their ${}^{18}\beta$ and ${}^{17}\kappa$ values:

$${}^{17}\theta_{\mathrm{A/B}}(T) = {}^{17}\kappa_{\mathrm{A}}(T) + \left[{}^{17}\kappa_{\mathrm{A}}(T) - {}^{17}\kappa_{\mathrm{B}}(T)\right]\left[\frac{\ln {}^{18}\beta_{\mathrm{B}}(T)}{\ln {}^{18}\beta_{\mathrm{A}}(T) - \ln {}^{18}\beta_{\mathrm{B}}(T)}\right]. \tag{11}$$

Similar to previous studies (e.g., Cao and Liu, 2011; Hayles et al., 2018; Schauble and Young, 2021), we report all results as ${}^{18}\beta(T)$ and ${}^{17}\kappa(T)$ rather than reporting ${}^{18}\alpha_{\mathrm{A/B}}(T)$ and ${}^{17}\theta_{\mathrm{A/B}}(T)$ directly.

2.3. Corrections to the B-GM-U equation

The approximations required to derive the B-GM-U equation can lead to large deviations between predicted and experimental equilibrium fractionation factors; several studies have thus proposed RPFR correction terms to reduce this inaccuracy (e.g., Richet et al., 1977; Liu et al., 2010; Zhang and Liu, 2018; Schauble and Young, 2021). Theoretical corrections generally fall into one of three categories: (i) deviations from the rigid rotor approximation, including quantum mechanical rotation corrections, centrifugal distortion, and torsion effects (Liu et al., 2010); (ii) deviations from the harmonic oscillator approximation, including anharmonic vibrational energy-state corrections and double-well potentials (Liu et al., 2010; Schauble and Young, 2021); and (iii) coupling, including vibration-rotation coupling and electron-nuclear coupling (i.e., deviations from the Born-Oppenheimer approximation; Born and Huang, 1954; Liu et al., 2010; Zhang and Liu, 2018).

As has been done previously, we ignore corrections of categories (i) and (iii) throughout this study. Specifically, Liu et al. (2010) have shown using a suite of gaseous compounds that all deviations from the rigid rotor approximation for rotational RPFRs, as well as vibration-rotation coupling, negligibly impact ${}^{*}\beta(T)$ estimates for non-hydrogen elements, including oxygen. Similarly, while inaccuracies due to deviations from the Born-Oppenheimer approximation can become significant at ultra-cold temperatures and for hydrogen-isotope fractionation, their impacts on ${}^{18}\beta(T)$ and ${}^{17}\beta(T)$ are likely small at temperatures relevant to Earth-surface conditions. For example, Zhang and Liu (2018) predict that the Born-Oppenheimer approximation leads to an over-estimate of ${}^{18}\alpha$ between gas-phase H_2O and SO_3 of 1.7 ‰ at −25 °C and that this offset decreases with increasing temperature. While not negligible, this inaccuracy is well within the experimental ${}^{18}\alpha(T)$ uncertainty for many species studied here (c.f., Lloyd, 1968; Chiba et al., 1981; Müller et al., 2013a; Wankel et al., 2014; Goldberg, 2021).

For category (ii) errors, Liu et al. (2010) predict that anharmonic corrections to the zero-point energy (ZPE) of vibration have an appreciable impact on ${}^{*}\beta(T)$ estimates for non-hydrogen elements, whereas anharmonic corrections

to excited vibrational states do not. Furthermore, Schauble and Young (2021) recently concluded that double-well vibrational potentials—which are present in hydrogen-bonding solutions such as water—do not influence $\Delta'^{17}O(T)$ by more than 0.01 ‰. We therefore ignore corrections for anharmonic excited states and double-well potentials, but we do incorporate anharmonic ZPE effects using a modified B-GM-U equation. Specifically, if the anharmonic ZPE is estimated or quantified directly, then the ZPE partition functions can be removed from the RPFR product and Eq. 6 can be rewritten as

$$^{*}\beta_{\mathrm{AnZPE}}(T) = \frac{s}{s^{*}}\left[\frac{e^{-z^{*}(T)}}{e^{-z(T)}}\right]_{\mathrm{ZPE}}\prod_{i=1}^{3n-x}\left[\frac{u_i^{*}(T)}{u_i(T)}\right]_{\mathrm{TR}}\left[\frac{1-e^{-u_i(T)}}{1-e^{-u_i^{*}(T)}}\right]_{\mathrm{EXC}}, \tag{12}$$

where

$$z(T) = \frac{h\zeta}{k_B T}, \tag{13}$$

ζ is the anharmonic ZPE, and the subscript "AnZPE" indicates that the result includes anharmonic ZPE corrections. Importantly, while anharmonic ZPE effects can influence $^{18}\beta(T)$ at the permil level, the impact on $\Delta\Delta'^{17}O(T)$ estimates is negligible due to error cancellation in $^{18}\beta(T)$ and $^{17}\beta(T)$ (c.f., Cao and Liu, 2011). We will therefore use Eq. 12 to calculate all $^{18}\beta(T)$ values and Eq. 6 to calculate all $^{17}\kappa(T)$ values used throughout this study (see Sec. 4.1 for details).

2.4. Computational corrections

In practice, direct determination of ζ values for sulfoxyanions is not feasible due to computational constraints. Instead, anharmonic ZPEs for large molecules and/or explicitly solvated anions are commonly estimated by multiplying harmonic ZPEs by empirical scaling factors (e.g., Irikura et al., 2009; Li et al., 2009). Here, scaling factors are calculated as the ratio of ZPEs determined for ideal gaseous ("*in vacuo*") sulfoxy species with and without anharmonic corrections (Liu et al., 2010; Eldridge et al., 2016); this practice is computationally efficient and leads to sub-permil propagated uncertainty in resulting $^{*}\beta_{\mathrm{AnZPE}}(T)$ values (Irikura et al., 2009).

Computational constraints additionally require that less accurate methods are used when analyzing large molecules—including explicitly solvated anions—resulting in ω values that are systematically biased (Irikura et al., 2005). These biases can be partially corrected by empirically scaling sulfoxyanion ω values to those determined using highly accurate methods (e.g., Scott and Radom, 1996; Merrick et al., 2007).[1] Similar to anharmonic ZPE scaling factors, here we calculate methodological scaling factors as the ratio of ω values for gaseous sulfoxy species determined using several computational theories and basis sets; we report all scaled results with the subscript "Sc". An analogous approach was used in a previous theoretical estimate of ^{18}O fractionation between SO_4^{2-} and water; it was shown to reduce the misfit between theoretical experimental results by several permil, highlighting the importance of methodological scaling factors when determining $^{18}\beta(T)$ values (Zeebe, 2010).

[1] This differs from the common practice of scaling *harmonic* to *fundamental* frequencies, which are inappropriate for the B-GM-U equation (see Liu et al., 2010, for details).

Finally, because ω and ZPE values are related to electron density, it is reasonable to hypothesize that scaling factors depend on sulfur-atom(s) redox state(s). This hypothesis is confirmed by Eldridge et al. (2016), who observed a larger anharmonic ZPE correction for *in vacuo* species in the S(+VI) redox state relative to more reduced species. As detailed in Sections 3 and 4, we therefore explore the effect of redox-specific methodological and anharmonic ZPE scaling factors on resulting ${}^{*}\beta_{\mathrm{Sc}}(T)$ and ${}^{*}\beta_{\mathrm{AnZPE}}(T)$ values for sulfoxyanions.

3. Methods

All ZPEs and harmonic frequencies were estimated using the computational chemistry software Gaussian 16 on the Research Computing cluster at Harvard University (Frisch et al., 2016). For all species, geometry optimizations were performed first, followed by isotope-specific frequency calculations. The masses of all atoms other than the oxygen atom of interest were assumed to equal their respective major isotopes (i.e., ^{1}H, ^{16}O, and ^{32}S). For species with several possible isotopomers (e.g., isotopic substitution at each O atom in SO_4^{2-}), frequencies were calculated individually for each isotopomer, and resulting ${}^{*}\beta(T)$ values were subsequently averaged. After each step, convergence was ensured by confirming that stationary points were found (i.e., that no imaginary frequencies exist).

All optimization and frequency calculations were performed using one of three methods of varying accuracy: (i) B3LYP/6-31+G(d,p) (Lee et al., 1988; Becke, 1993), (ii) CCSD/aug-cc-pVTZ (Scuseria et al., 1988; Kendall et al., 1992), and (iii) MP2/aug-cc-pVTZ (Møller and Plesset, 1934; Frisch et al., 1990; Kendall et al., 1992). Method (i) is a low/moderate-complexity hybrid of Hartree-Fock (HF) and density functional theory (DFT) with a double-zeta Pople basis set, including diffuse and polarization functions. It has been used previously to estimate multiple-sulfur isotope fractionation factors of sulfoxyanions (Eldridge et al., 2016) and elemental sulfur compounds (Eldridge et al., 2021); similar methods have additionally been used to estimate triple-oxygen isotope fractionation factors for a range of gaseous and mineral species (Cao and Liu, 2011; Hayles et al., 2018). Here, we applied method (i) to all gaseous and aqueous species, including anharmonic ZPE corrections for gaseous species. Method (ii) is a high-complexity coupled cluster HF theory with a correlation-consistent polarized triple-zeta basis set, augmented with diffuse functions. It is a highly accurate but computationally expensive method and was used here for gaseous species to estimate the effect of basis-set accuracy on fractionation factor results (i.e., to calculate methodological scaling factors). Method (iii) utilizes second-order Møller-Plesset perturbation theory with the same basis set used in method (ii). Like method (ii), it is highly accurate yet computationally expensive; however, unlike method (ii), it additionally allows for anharmonic corrections because the analytic second derivatives can be calculated (Frisch et al., 1990, 2016). This method was used here for gaseous species to estimate the effect of basis-set accuracy as well as anharmonic ZPE corrections on fractionation factor results (i.e., to calculate methodological and anharmonic ZPE scaling factors), as has been done previously (Liu et al., 2010).

3.1. Gaseous species computations

To estimate methodological and anharmonic-ZPE scaling factors and their effect on isotope fractionation-factor estimates, several gaseous sulfoxy species of varying sulfur redox states were analyzed: (i) $SO_{3(g)}$ [S(+VI)], (ii) $SO_{2(g)}$ [S(+IV)], (iii) $S_2O_{2(g)}$ and $SO_{(g)}$ [S(+II)], (iv) $S_{3(g)}$ and $S_{2(g)}$ [S(0), elemental], (v) $H_2S_{(g)}$ [S(-II)], (vi) $(S)SO_{2(g)}$ [mixed valence S(-I)/S(+V)]; water vapor, $H_2O_{(vap.)}$, and molecular oxygen, $O_{2(g)}$ were additionally analyzed (Fig. S.1). Harmonic frequencies and ZPEs for all gaseous species were calculated using all three methods, and anharmonic ZPEs were calculated using B3LYP/6-31+G(d,p) and MP2/aug-cc-pVTZ methods.

3.2. Liquid water computations

Liquid water harmonic frequencies and ZPEs were calculated following the procedure of Hayles et al. (2018) using the B3LYP/6-31+G(d,p) method. First, water "droplets" were generated by starting with 6 H_2O molecules and iteratively performing a geometry optimization followed by the addition of 4 more H_2O molecules until a final cluster size of 30 H_2O molecules was achieved. Such iterative optimizations are commonly performed to ensure that water droplet geometry remains stable (e.g., Li et al., 2009; Zeebe, 2010; Li and Liu, 2011; Eldridge et al., 2016). Then, each H_2O molecule was individually isotopically substituted and harmonic frequencies and ZPEs were determined, yielding $n = 30$ sets of frequencies. Finally, to minimize the influence of water droplet cluster geometry on resulting ${}^{*}\beta(T)$ values, the whole procedure was repeated 4 more times with arbitrary molecular geometries for a total of $n = 5$ water droplets.

3.3. Aqueous sulfoxyanion computations

Aqueous sulfoxyanion harmonic frequencies and ZPEs were calculated following the procedure of Eldridge et al. (2016) using the B3LYP/6-31+G(d,p) method. Several isomers at each redox state were considered: (i) $SO_4{}^{2-}$ and $SO_3(OH)^-$ [S(+VI), collectively termed "sulfate species"]; (ii) $SO_3{}^{2-}$, $(HS)O_3{}^-$, $SO_2(OH)^-$, and dissolved $SO_{2(aq.)}$ gas [S(+IV), collectively termed "sulfite species"]; (iii) $SO_2{}^{2-}$, $(HS)O_2{}^-$, $SO(OH)^-$, (HS)O(OH), and $S(OH)_2$ [S(+II), collectively termed "sulfoxylate species"]; and finally (iv) $S_2O_3{}^{2-}$, $(HS)SO_3{}^-$, and $S_2O_2(OH)^-$ [mixed valence S(-I)/S(+V), collectively termed "thiosulfate species"] (Fig. 1). Like liquid water calculations, all sulfoxyanions were analyzed using the water "droplet" method (Li et al., 2009; Li and Liu, 2011). Droplets were generated by starting with the sulfoxyanion of interest and 6 H_2O molecules; geometry optimizations and subsequent H_2O additions were performed until a final cluster size of $n = 30$ H_2O molecules was reached. Special care was taken to monitor sulfoxyanion $-$OH bond lengths, as geometric instabilities could lead to deprotonation, particularly for highly acidic species. To estimate isotope fractionation uncertainty resulting from droplet geometry and stretched $-$OH bonds, both $SO_3(OH)^-$ and $S_2O_2(OH)^-$ water droplet geometries were determined in triplicate.

3.4. Sources of uncertainty and statistical methods

There exist three main potential sources of uncertainty and/or bias: (i) assumptions required to derive the B-GM-U equation (Sec. 2.2-2.3); (ii) approximations inherent to the particular computational theory and basis set used to model

the molecular system, including methodological scaling factor uncertainty (Sec. 2.4); and (iii) variability due to water droplet geometry, for example due to the importance of water dimers and trimers at higher temperature (Eldridge et al., 2016; Hayles et al., 2018). To assess points (i) and (ii), we empirically estimate methodological harmonic scaling factors and anharmonic ZPE scaling factors for a suite of gaseous sulfoxy compounds using several theories and basis sets (e.g., following Liu et al., 2010; Cao and Liu, 2011). To assess point (iii), we determine triplicate water droplet geometries for a subset of sulfoxyanion species [$SO_3(OH)^-$ and $S_2O_2(OH)^-$]. We additionally calculate semi-empirical liquid water ${}^*\beta(T)$ values following the method of Hayles et al. (2018) since theoretical results may not fully capture liquid water molecular interactions.

Finally, we assess the overall accuracy of our results by comparing predicted ${}^{18}\alpha_{A/H_2O(liq.)}(T)$ with all existing theoretical and experimental results from the literature, where "A" is the sulfoxyanion of interest (Lloyd, 1968; Chiba et al., 1981; Zeebe, 2010; Müller et al., 2013a; Wankel et al., 2014; Goldberg, 2021). Unfortunately, no experimental equilibrium $\Delta\Delta'^{17}O_{A/H_2O(liq.)}(T)$ estimates currently exist for sulfoxyanions. However, as mentioned previously, theoretical $\Delta\Delta'^{17}O_{A/H_2O(liq.)}(T)$ error has been shown to be small (i.e., less than analytical uncertainty)—even if ${}^{18}\alpha_{A/H_2O(liq.)}(T)$ is in error by several permil—due to mass-dependent error cancellation (Cao and Liu, 2012). We therefore assume that theoretical $\Delta\Delta'^{17}O_{A/H_2O(liq.)}(T)$ predictions are accurate if the corresponding ${}^{18}\alpha_{A/H_2O(liq.)}(T)$ agrees with experimental results to within several permil.

All regressions (e.g., when calculating methodological and anharmonic ZPE scaling factors) were performed using orthogonal distance regression, which allows for uncertainty in both x and y variables. Regression results are reported with $\pm 1\sigma$ uncertainty. Statistical differences between populations were determined using a two-way analysis of variance (ANOVA) and evaluated at the $p = 0.05$ level. Misfit between theoretical predictions and experimental results was determined as the root mean square error (RMSE); to estimate bulk solution fractionation for each experiment, "mean" fractionation factors were calculated as the average of all isomers weighted by their pH-specific relative abundance.

4. Results

Predicted bond lengths and angles for all gaseous species using all methods are reported in Table S.1, whereas calculated ZPEs and harmonic frequencies are reported in Table S.2. Similarly, predicted bond lengths and angles for aqueous sulfoxyanions are reported in Table S.3, whereas ZPEs and harmonic frequencies are reported in Table S.4. All optimization and frequency results, as well as python scripts used to calculate all ${}^*\beta(T)$, ${}^{17}\kappa(T)$, ${}^{18}\alpha$ and $\Delta'^{17}O$ values, are included in the Supplementary Data.

4.1. Gaseous species and scaling factors

For gaseous species, all methods result in similar optimized geometries with slight differences in bond lengths and angles. Bond length differences between methods reach a maximum of 0.12 Å (for S – S in $S_2O_{2(g)}$) and average 0.03

Å, with MP2/aug-cc-pVTZ consistently predicting the longest bonds and CCSD/aug-cc-pVTZ consistently predicting the shortest bonds. Bond angle differences between methods are similarly small, reaching a maximum of 6.1° (for O−S−S in $S_2O_{2(g)}$) and averaging 1.3° with no clear trend between methods.

When considering all gaseous species together, ω values predicted by the CCSD/aug-cc-pVTZ method are nearly identical to experimental results for all compounds reported in Johnson III (2020), with an experimental vs. theoretical regression slope of 1.0062 ± 0.0002 (r^2 = 0.9999; Fig. S.2A). Similarly, ω predictions using the MP2/aug-cc-pVTZ method are generally nearly identical to experimental values; however, all diatomic molecules (SO, S_2, and O_2) deviate significantly from this trend, with predicted values consistently lower than experimental results. Omitting the diatomic compounds, this method yields an experimental vs. theoretical regression slope of 1.0016 ± 0.0002 (r^2 = 0.9992; Fig. S.2B). Both methods yield slightly higher ω values than those predicted by the B3LYP/6-31+G(d,p) method, with resulting all-compound average methodological scaling factors of 1.0256 ± 0.0002 for CCSD/aug-cc-pVTZ (r^2 = 0.9991; Fig. S.2C) and 1.0173 ± 0.0002 for MP2/aug-cc-pVTZ (omitting diatomic molecules; r^2 = 0.9992; Fig. S.2D). When separating compounds by redox state, methodological scaling factors range from 1.0093 to 1.0764 for CCSD/aug-cc-pVTZ (Fig. S.2E) and from 0.9840 to 1.0830 for MP2/aug-cc-pVTZ (Fig. S.2F). For CCSD/aug-cc-pVTZ, scaling factors monotonically increase with increasing sulfur-atom redox state (treating mixed-valence (S)$SO_{2(g)}$ as S(+V) since this is the redox state of the O-bound sulfonate atom). In contrast, MP2/aug-cc-pVTZ scaling factors display no such trend, with a maximum for S(0) compounds and a minimum for S(+IV) compounds.

When considering all species together, anharmonic ZPE values predicted by the B3LYP/6-31+G(d,p) and MP2/aug-cc-pVTZ methods are slightly lower than their harmonic counterparts, yielding all-compound average anharmonic ZPE scaling factors of 0.9891 ± 0.0002 (r^2 = 1.0000; Fig. S.3A) and 0.9901 ± 0.0002 (omitting diatomic molecules; r^2 = 0.9999; Fig. S.3B), respectively. When separated by redox state, anharmonic ZPE scaling factors range from 0.9872 to 0.9976 for B3LYP/6-31+G(d,p) (Fig. S.3C) and from 0.9848 to 1.0012 for MP2/aug-cc-pVTZ (Fig. S.3D). However, when only considering sulfoxy species [i.e., S(+II) through S(+VI) redox states], scaling factors are essentially identical across redox state, ranging from 0.9953 to 0.9967 for B3LYP/6-31+G(d,p) and from 0.9963 to 1.0012 for MP2/aug-cc-pVTZ. Both methods similarly predict anharmonic-corrected fundamental frequencies, ν, near the experimental values reported in Johnson III (2020), yielding experimental vs. predicted regression slopes of 0.9864 ± 0.0002 for B3LYP/6-31+G(d,p) (r^2 = 0.9993; Fig. S.4A) and 1.0020 ± 0.0002 for MP2/aug-cc-pVTZ (omitting diatomic molecules; r^2 = 0.9993; Fig. S.4B). Unlike for these methods, fundamental frequencies and anharmonic ZPE corrections cannot be determined for CCSD/aug-cc-pVTZ since analytic second derivatives cannot be calculated (Scuseria et al., 1988; Frisch et al., 2016).

Resulting $^{18}\beta_h(T)$ values determined using unscaled harmonic frequencies (Eq. 6) for all gaseous sulfoxy species, $H_2O_{(vap.)}$, and $O_{2(g)}$ are shown in Fig. S.5. For all methods at a given temperature, sulfoxy species $^{18}\beta_h(T)$ values generally increase with increasing sulfur redox state. For example, $^{18}\beta_h(T)$ calculated at 25 °C using the B3LYP/6-31+G(d,p) method increase from 1.0738 for $S_2O_{2(g)}$ to 1.0947 for $SO_{3(g)}$; $H_2O_{(vap.)}$ and $O_{2(g)}$ predictions generally

lie between those of S(+II) and S(+IV) species. For a given compound, the CCSD/aug-cc-pVTZ method predicts the highest $^{18}\beta_{h}(T)$ at all temperatures, with B3LYP/6-31+G(d,p) and MP2/aug-cc-pVTZ both predicting lower—yet similar—values. For example, $^{18}\beta_{h}(T)$ calculated at 25 °C for $SO_{3(g)}$ ranges from 1.0947 using B3LYP/6-31+G(d,p) to 1.1065 using CCSD/aug-cc-pVTZ. For all compounds using all methods, $^{18}\beta_{h}(T)$ values approach unity with increasing temperature, as expected (i.e., no fractionation as $T \rightarrow \infty$).

Methodological scaling factor corrections to B3LYP/6-31+G(d,p) results are shown in Fig. S.6. When considering the all-compound average scaling factors, $^{18}\beta_{sc}(T)$ values at 25 °C only differ from their $^{18}\beta_{h}(T)$ counterparts by a maximum of 3.6 ‰ using CCSD/aug-cc-pVTZ scaling and 2.4 ‰ using MP2/aug-cc-pVTZ scaling [both maxima correspond to $SO_{3(g)}$]. In contrast, redox-state specific methodological scaling factors yield $^{18}\beta_{sc}(T)$ corrections at 25 °C that range from 0.7 ‰ [$H_2O_{(vap.)}$] to 10.4 ‰ [$SO_{3(g)}$] using CCSD/aug-cc-pVTZ and from −2.0 ‰ [$SO_{2(g)}$] to 5.9 ‰ [(S)$SO_{2(g)}$] using MP2/aug-cc-pVTZ. Interestingly, $SO_{2(g)}$ scaling factors using the MP2/aug-cc-pVTZ method are consistently ≤ 1 for all T; in contrast, all other methodological scaling factors are always ≥ 1. Like $^{18}\beta_{h}(T)$ results, all methodological scaling factors approach unity with increasing temperature.

Anharmonic ZPE scaling factor corrections to $^{18}\beta_{h}(T)$ values (Eq. 12) calculated using B3LYP/6-31+G(d,p) and MP2/aug-cc-pVTZ methods are shown in Fig. S.7. When using all-compound average scaling factors, $^{18}\beta_{AnZPE}(T)$ corrections at 25 °C range from −1.8 ‰ [$SO_{3(g)}$] to −0.8 ‰ [$H_2O_{(vap.)}$] for B3LYP/6-31+G(d,p) and from −1.6 ‰ [$SO_{3(g)}$] to −0.7 ‰ [$H_2O_{(vap.)}$] for MP2/aug-cc-pVTZ. Unlike methodological scaling factors, anharmonic ZPE scaling factors are similar in magnitude when using all-compound average and redox-state specific values. However, the scaling-factor order between compounds is different for all-compound average and redox-state specific results. For example, redox-state specific scaling factors range from −1.0 ‰ [$O_{2(g)}$] to −0.3 ‰ [$SO_{(g)}$] for B3LYP/6-31+G(d,p) and from −1.3 ‰ [$O_{2(g)}$] to 0.1 ‰ [$SO_{(g)}$] for MP2/aug-cc-pVTZ. Interestingly, S(+II) anharmonic ZPE scaling factors calculated using MP2/aug-cc-pVTZ are consistently ≥ 1, unlike all other results. Similar to $^{18}\beta_{h}(T)$ and methodological scaling factor results, all anharmonic ZPE scaling factors approach unity with increasing temperature.

Based on these results, we choose to scale aqueous-phase ω and ZPE values using the redox-state specific CCSD/aug-cc-pVTZ methodological scaling factors and the redox-state specific B3LYP/6-31+G(d,p) anharmonic ZPE scaling factors when calculating $^{18}\beta_{sc,AnZPE}(T)$. The reason for choosing CCSD/aug-cc-pVTZ rather than MP2/aug-cc-pVTZ scaling factors is two-fold: (i) MP2/aug-cc-pVTZ ω and ν values for diatomic molecules are offset from experimental results (Fig. S.2, S.4), and (ii) MP2/aug-cc-pVTZ methodological and anharmonic ZPE scaling factors do not follow the expected trend with sulfur redox-state (Fig. S.2-S.3). Furthermore, redox-state specific scaling factors yield much closer agreement with experimental results than do all-compound average scaling factors (i.e., lower RMSE), particularly for sulfate and sulfite species (Sec. 4.3–4.6). Overall scaling factor results for all gaseous sulfoxy species, $H_2O_{(vap.)}$, and $O_{2(g)}$—including both methodological and anharmonic ZPE effects—are shown in Fig. S.8. Additionally, following common practice, seventh-order polynomial fits for calculating $^{18}\beta_{sc,AnZPE}(T)$ for $H_2O_{(vap.)}$ and $O_{2(g)}$ at any arbitrary temperature are reported in Table 1.

Resulting $^{17}\kappa_{h}(T)$ values calculated using unscaled harmonic frequencies (Eq. 6) for all gaseous sulfoxy species,

$H_2O_{(vap.)}$, and $O_{2(g)}$ are shown in Fig. S.9. For all methods at all temperatures, $H_2O_{(vap.)}$ consistently displays the highest $^{17}\kappa_h(T)$ values, whereas all other compounds cluster at lower values. For example, the B3LYP/6-31+G(d,p) method at 25 °C predicts a $^{17}\kappa_h(T)$ value for $H_2O_{(vap.)}$ of 0.5300 with all other compounds ranging from 0.5282 [$SO_{2(g)}$] to 0.5283 [$S_2O_{2(g)}$]. For all compounds and all methods, $^{17}\kappa_h(T)$ values approach 0.5305 with increasing temperature, as predicted by the high-temperature theoretical limit (Eq. 10; Young et al., 2002)

Unlike for $^{18}\beta_{sc}(T)$ predictions, methodological scaling factors negligibly impact $^{17}\kappa_{sc}(T)$ values relative to their $^{17}\kappa_h(T)$ counterparts (Fig. S.10), as observed previously (Cao and Liu, 2011). For example, $^{17}\kappa_{sc}(T)$ offsets using the all-compound average scaling factors at 25 °C range from -5.9×10^{-5} [$SO_{(g)}$] to -3.2×10^{-6} [$H_2O_{(vap.)}$] for CCSD/aug-cc-pVTZ and from -4.0×10^{-5} [$SO_{(g)}$] to -2.2×10^{-6} [$H_2O_{(vap.)}$] for MP2/aug-cc-pVTZ. Offsets reach slightly larger values when using redox-state specific scaling factors, but still only range from -1.6×10^{-4} [(S)$SO_{2(g)}$] to -1.2×10^{-6} [$H_2O_{(vap.)}$] for CCSD/aug-cc-pVTZ and from -9.3×10^{-5} [(S)$SO_{2(g)}$] to 3.6×10^{-5} [$SO_{2(g)}$] for MP2/aug-cc-pVTZ.

Similarly, anharmonic ZPE scaling factors lead to only small offsets between $^{17}\kappa_{AnZPE}(T)$ and $^{17}\kappa_h(T)$ (Fig. S.11). For example, differences between $^{17}\kappa_{AnZPE}(T)$ and $^{17}\kappa_h(T)$ values at 25 °C using the all-compound average scaling factors range from -2.1×10^{-4} [$SO_{3(g)}$] to 1.6×10^{-4} [$O_{2(g)}$] for B3LYP/6-31+G(d,p) and from -1.4×10^{-4} [$H_2O_{(vap.)}$] to 1.5×10^{-4} [$SO_{2(g)}$] for MP2/aug-cc-pVTZ. Unlike all other variables, all-compound average and redox-state specific anharmonic ZPE scaling factors yield nearly identical $^{17}\kappa_{AnZPE}(T)$ corrections. However, anharmonic ZPE corrections also lead to diverging predictions with increasing temperature. That is, $^{17}\kappa_{AnZPE}(T)$ does not converge on 0.5305 as $T \to \infty$, as is theoretically predicted (Eq. 10; Young et al., 2002). As detailed in Cao and Liu (2011), this results from the fact that $\ln(^{18}\beta_{AnhC})/\ln(^{17}\beta_{AnhC}) \neq 0.5305$, where "AnhC" refers only to the contribution due to anharmonic ZPE correction (i.e., the $z(T)$ term in Eq. 12).

Because methodological scaling factor corrections are negligible and because anharmonic ZPE scaling factors lead to diverging $^{17}\kappa_{AnZPE}(T)$ values with increasing temperature, we choose not to scale ω values when calculating $^{17}\kappa_h(T)$ for all aqueous-phase compounds reported in this study (i.e., results are calculated using Eq. 6). Resulting seventh-order polynomial fits for calculating $^{17}\kappa_h(T)$ for $H_2O_{(vap.)}$ and $O_{2(g)}$ at any arbitrary temperature are reported in Table 2.

4.2. Liquid water

Calculated $^{18}\beta_{sc,AnZPE}(T)$ and $^{17}\kappa_h(T)$ values display some variability for individual water molecule isotope substitutions; however, cluster-average values for each water droplet are identical across all temperatures ($n = 5$; Fig. S.12). Results therefore suggest minimal variability due to droplet geometry. Still, to account for effects that are not captured by the water droplet method, we additionally calculate "semi-empirical" (subscript "se") liquid water $^{18}\beta_{se}(T)$ and $^{17}\kappa_{se}(T)$ values following Hayles et al. (2018). First, we combine theoretical $^{18}\beta_{sc,AnZPE}(T)$ values for $H_2O_{(vap.)}$ calculated using the B3LYP/6-31+G(d,p) method with empirically measured $^{18}\alpha_{liq./vap.}(T)$ from Horita et al. (2008) (their Eq. 20) to determine $^{18}\beta_{se}(T)$ for $H_2O_{(liq.)}$ using Eq. 8. We then calculate $^{17}\alpha_{liq./vap.}(T)$ as a function

of ${}^{18}\alpha_{\text{liq./vap.}}(T)$ and ${}^{17}\theta_{\text{liq./vap.}}(T)$ using Eq. 3. However, ${}^{17}\theta_{\text{liq./vap.}}(T)$ has not yet been empirically determined with sufficient precision across the entire temperature range of interest (c.f., Barkan and Luz, 2005). We therefore theoretically estimate ${}^{17}\theta_{\text{liq./vap.}}(T)$ using ${}^{18}\beta_{\text{sc,AnZPE}}(T)$ and ${}^{17}\kappa_{\text{h}}(T)$ values calculated with the B3LYP/6-31+G(d,p) method for $H_2O_{(liq.)}$ and $H_2O_{(vap.)}$ following Eq. 11. Resulting theoretical ${}^{17}\theta_{\text{liq./vap.}}(T)$ agrees with available empirical results to within 2.0×10^{-4}, suggesting that our predictions are robust (Fig. S.13; Barkan and Luz, 2005). We then determine ${}^{17}\beta_{\text{se}}(T)$ for $H_2O_{(liq.)}$ as:

$$ {}^{17}\beta_{\text{se}}(T) = \left({}^{18}\alpha_{\text{liq./vap.}}(T)\right)^{{}^{17}\theta_{\text{liq./vap.}}(T)} \times {}^{17}\beta_{\text{sc,AnZPE}}(T), \tag{14} $$

where ${}^{17}\beta_{\text{sc,AnZPE}}(T)$ here refers to the values for $H_2O_{(vap.)}$ calculated using the B3LYP/6-31+G(d,p) method. Finally, ${}^{17}\kappa_{\text{se}}(T)$ is determined following Eq. 9. To test the influence of salinity on resulting fractionations, we additionally repeat this process using empirically measured ${}^{18}\alpha_{\text{liq./vap.}}(T)$ values for a 4 M NaCl solution from Horita et al. (1995) (their Eq. 10).

Resulting freshwater ${}^{18}\beta_{\text{se}}(T)$ calculated here only deviates from pure theoretical predictions by a maximum of 0.8 ‰ and from semi-empirical values reported in Hayles et al. (2018) by a maximum of 3.1 ‰ (Fig. S.13A). Similarly, freshwater ${}^{17}\kappa_{\text{se}}(T)$ agrees with theoretical results and with semi-empirical results of Hayles et al. (2018) to within 1.0×10^{-4}, indicating that isotope effects not captured by the water droplet method are small (Fig. S.13B). Furthermore, salinity exhibits a negligible effect on both ${}^{18}\beta_{\text{se}}(T)$ and ${}^{17}\kappa_{\text{se}}(T)$, leading to maximum deviations from freshwater results of only 0.4 ‰ and $<1 \times 10^{-6}$, respectively. We therefore use freshwater ${}^{18}\beta_{\text{se}}(T)$ and ${}^{17}\kappa_{\text{se}}(T)$ when calculating all sulfoxyanion fractionation factors below (Sec. 4.3–4.6). Nonetheless, seventh-order polynomial fits for calculating theoretical, semi-empirical (freshwater), and semi-empirical (saline) ${}^{18}\beta(T)$ and ${}^{17}\kappa(T)$ values at any arbitrary temperature are reported in Tables 1–2.

4.3. Aqueous sulfate species

On average, sulfate species geometries are similar to those calculated by Eldridge et al. (2016), with bond lengths differing by a maximum of 0.01 Å and angles differing by a maximum of 3.1° (Fig. 1; Table S.3). Replicate $SO_3(OH)^-$ geometries calculated here show nearly identical S–O bond lengths, differing by only 0.01 Å. However, replicate S–(OH) and O–H bond lengths differ by up to 0.10 Å and 0.09 Å; similarly, O–S–O, O–S–(OH), and S–O–H bond angles differ by up to 4.0°, 4.2°, and 6.4° between replicates, likely due to the influence of H_2O geometry on hydrogen bond length and angle. Despite these geometric differences, ${}^{18}\beta_{\text{sc,AnZPE}}(T)$ and ${}^{17}\kappa_{\text{h}}(T)$ are nearly identical across replicates (Fig. 2). This leads to standard deviations in ${}^{18}\alpha_{SO_3(OH)^-/H_2O(liq.)}(T)$ and $\Delta\Delta'{}^{17}O_{SO_3(OH)^-/H_2O(liq.)}(T)$ of only ±0.6 ‰ and ±0.002 ‰ at 25 °C (n = 3; Fig. 3), which is near typical analytical precision. Seventh-order polynomial fits for calculating ${}^{18}\beta_{\text{sc,AnZPE}}(T)$ and ${}^{17}\kappa_{\text{h}}(T)$ values (replicate average results for $SO_3(OH)^-$) are reported in Tables 1–2.

Resulting ${}^{18}\alpha_{SO_4{}^{2-}/H_2O(liq.)}(T)$ and ${}^{18}\alpha_{SO_3(OH)^-/H_2O(liq.)}(T)$ values are in close agreement with all experimental data as well as the only previous theoretical study performed to date (Table S.5; Lloyd, 1968; Chiba et al., 1981; Zeebe, 2010). Comparing experimental results to $SO_4{}^{2-}$ predictions yields an RMSE of 4.7 ‰, much larger than expected

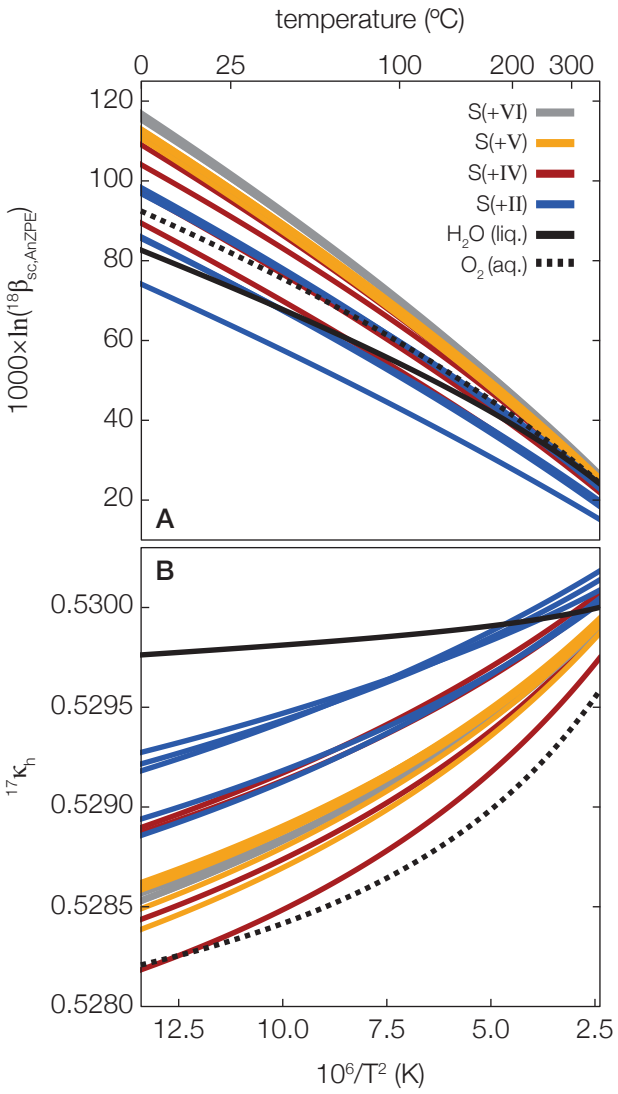

Figure 2: **Calculated $^{18}\beta_{\mathbf{sc,AnZPE}}(T)$ and $^{17}\kappa_{\mathbf{h}}(T)$ values for all oxygen-containing solvated species.** (**A**) Scaled- and anharmonic ZPE-corrected partition function ratios [i.e., $^{18}\beta_{\mathrm{sc,AnZPE}}(T)$] and (**B**) harmonic triple-oxygen partition function ratios [i.e., $^{17}\kappa_{\mathrm{h}}(T)$] plotted as a function of temperature. Line styles refer to each species or sulfur redox state: solid black = $H_2O_{(liq.)}$, dotted black = $O_{2(aq.)}$, blue = sulfoxylate species, S(+II); red = sulfite species, S(+IV); yellow = thiosulfate species, S(+V) (sulfonate group); gray = sulfate species, S(+VI). All isomers within a given sulfur redox state are plotted with the same line styles.

analytical precision. However, this RMSE decreases substantially to 1.8 ‰ when comparing to $SO_3(OH)^-$, rather than $SO_4{}^{2-}$, predictions (Fig. 3A). Similar differences have been observed previously (Zeebe, 2010) and suggest that isotope exchange occurs via $SO_3(OH)^-$ rather than sulfate *sensu stricto*. This hypothesis is further supported by experimentally determined oxygen isotope exchange rates, which increase with decreasing pH and thus increasing

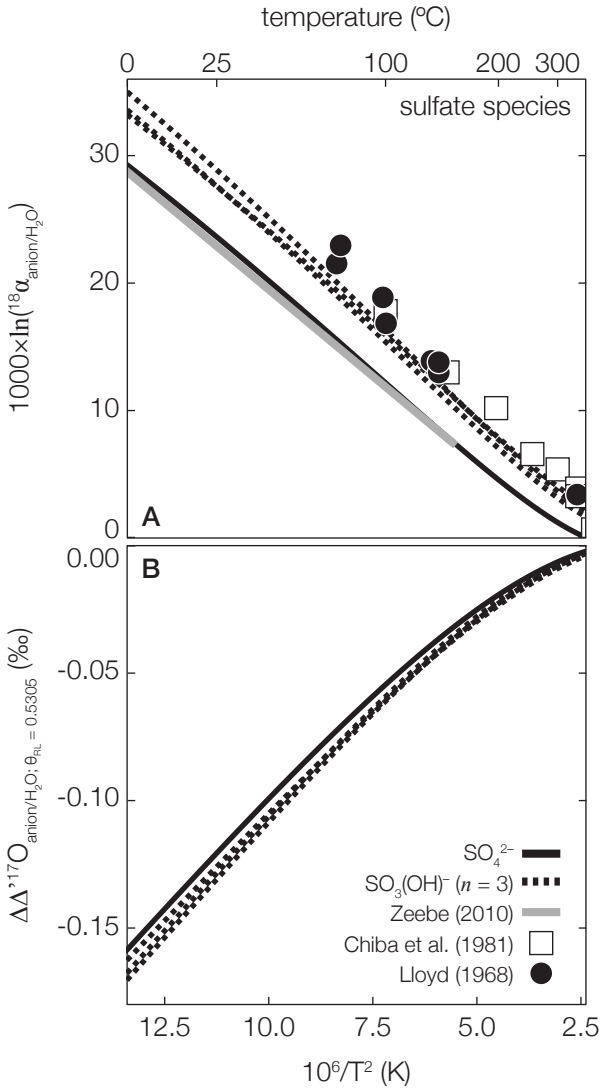

Figure 3: **Triple-oxygen equilibrium fractionation factors between liquid water and sulfate species.** Predicted (**A**) $1000 \times \ln(^{18}\alpha)(T)$ and (**B**) $\Delta\Delta'^{17}\mathrm{O}(T)$ between each sulfate species [SO_4^{2-}; $SO_3(OH)^-$, $n = 3$ replicates] and "semi empirical" liquid water using $^{18}\beta_{\mathrm{sc,AnZPE}}(T)$ and $^{17}\kappa_{\mathrm{h}}(T)$ values calculated by Tables 1-2. Also shown in panel (**A**): experimental results for dissolved sulfate over a range of pH conditions (Lloyd, 1968), experimental results for anhydrite mineral ($CaSO_4$) at high-pressure hydrothermal conditions (Chiba et al., 1981), and *ab initio* predictions for SO_4^{2-} calculated using the Hartree Fock method (Zeebe, 2010). Panel (**B**) values correspond to $^{17}\theta_{\mathrm{RL}} = 0.5305$ in the definition of $\Delta'^{17}\mathrm{O}$.

relative $SO_3(OH)^-$ abundance (Lloyd, 1968).

Importantly, $^{18}\alpha_{SO_4^{2-}/H_2O(liq.)}(T)$ values calculated here between 0 °C and 150 °C are in close agreement with predictions from Zeebe (2010) (their Eq. 5), exhibiting an RMSE of 0.5 ‰ (Fig. 3A). This agreement occurs despite

the conclusion by Zeebe (2010) that MP2 or B3LYP functionals yield unstable geometries and inaccurate scaling factors for hydrated SO_4^{2-}. However, the basis sets tested by Zeebe (2010) for B3LYP and MP2 functionals did not include hydrogen atom polarization functions, which are necessary to minimize basis set superposition error when using DFT methods for systems with hydrogen bonds (Novoa and Sosa, 1995). By including hydrogen atom polarization functions, our results never yielded unstable geometries (i.e., imaginary frequencies) for any sulfate species at any water droplet cluster size (Supplementary Data). Furthermore, the agreement between $^{18}\alpha(T)$ values predicted here with past experimental and theoretical results confirms our choice of methodological and anharmonic ZPE scaling factors. In contrast, the use of $^{18}\beta_{h}(T)$ would have led to $^{18}\alpha_{SO_4^{2-}/H_2O(liq.)}(T)$ and $^{18}\alpha_{SO_3(OH)^-/H_2O(liq.)}(T)$ predictions that differ from experimental and previous theoretical results by up to 10 ‰.

Currently, no experimental $\Delta\Delta'^{17}O(T)$ data exist with which we can compare our theoretical results. Still, predicted $\Delta\Delta'^{17}O_{SO_4^{2-}/H_2O(liq.)}(T)$ and $\Delta\Delta'^{17}O_{SO_3(OH)^-/H_2O(liq.)}(T)$ values are nearly identical across all temperatures, differing by a maximum of 0.008 ‰ at 0 °C (Fig. 3B). Interestingly, both species yield large negative $\Delta\Delta'^{17}O(T)$ predictions (i.e., $\Delta'^{17}O$ values less than that of surrounding water), reaching values as low as −0.167 ‰ at 0 °C. Predicted fractionations for both ^{18}O and ^{17}O decrease with increasing temperature, as expected.

4.4. Aqueous sulfite species

Similar to sulfate, sulfite species geometries calculated here are in close agreement with those reported in Eldridge et al. (2016), with bond lengths differing by a maximum of 0.03 Å and angles differing by a maximum of 2.5° (Fig. 1; Table S.3). However, unlike for sulfate species, there exist large differences in $^{18}\beta_{sc,AnZPE}(T)$ and $^{17}\kappa_{h}(T)$ between sulfite isomers (Fig. 2). Across all temperatures, $(HS)O_3^-$ consistently exhibits the highest $^{18}\beta_{sc,AnZPE}(T)$ values whereas SO_3^{2-} consistently exhibits the lowest values. In contrast, SO_3^{2-} displays the highest $^{17}\kappa_{h}(T)$ values whereas $SO_{2(aq.)}$ displays the lowest values. Seventh-order polynomial fits for calculating $^{18}\beta_{sc,AnZPE}(T)$ and $^{17}\kappa_{h}(T)$ values for all sulfite species are reported in Tables 1–2.

These differences in $^{18}\beta_{sc,AnZPE}(T)$ and $^{17}\kappa_{h}(T)$ lead to large differences in $^{18}\alpha(T)$ and $\Delta\Delta'^{17}O(T)$ predictions between different sulfite isomers and water (Fig. 4). For example, our results predict that $(HS)O_3^-$ is 17.7 ‰ more enriched than SO_3^{2-} when both are in equilibrium with water at 25 °C. Similarly, estimated $\Delta'^{17}O(T)$ for SO_3^{2-} is 0.083 ‰ higher than that for $SO_{2(aq.)}$ when both are in equilibrium with H_2O at 25 °C; still, all isomers display $\Delta'^{17}O(T)$ values lower than that of equilibrated water across all temperatures.

Interestingly, $^{18}\alpha_{SO_3^{2-}/H_2O(liq.)}(T)$ and $^{18}\alpha_{SO_2(OH)^-/H_2O(liq.)}(T)$ values calculated here reverse sign at 71 °C and 191 °C, respectively. Above these temperatures, we predict that SO_3^{2-} and $SO_2(OH)^-$ are more depleted in ^{18}O relative to H_2O. Similar crossovers have been observed previously for other oxygen-bearing species (e.g., Hayles et al., 2018). In contrast, all other isomers exhibit $^{18}\alpha(T)$ values as high as 26.4 ‰ at 0 °C and do not display crossover points. Unlike for $^{18}\alpha(T)$, $\Delta\Delta'^{17}O(T)$ predictions never exhibit crossover points and instead trend toward zero at high temperature for all isomers, as expected (Young et al., 2002).

Like for sulfate, all existing experimental sulfite $^{18}\alpha(T)$ results are in close agreement with predictions calculated

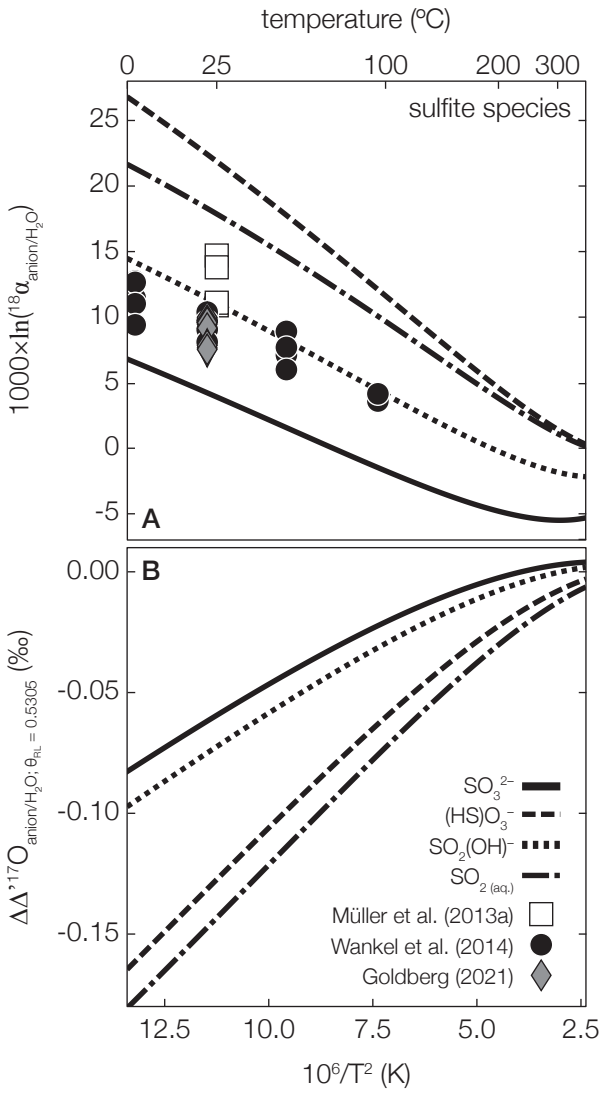

Figure 4: **Triple-oxygen fractionation factors between liquid water and sulfite species.** Predicted (**A**) $1000 \times \ln(^{18}\alpha)(T)$ and (**B**) $\Delta\Delta'^{17}\mathrm{O}(T)$ between each sulfite species [SO_3^{2-}, $(HS)O_3^-$, $SO_2(OH)^-$, and $SO_{2(aq.)}$] and "semi empirical" liquid water using $^{18}\beta_{sc,AnZPE}(T)$ and $^{17}\kappa_h(T)$ values calculated by Tables 1-2. Also shown in panel (**A**): experimental results for dissolved sulfite over a range of temperature and pH conditions from three laboratories (Müller et al., 2013a; Wankel et al., 2014; Goldberg, 2021). Panel (**B**) values correspond to $^{17}\theta_{RL} = 0.5305$ in the definition of $\Delta'^{17}\mathrm{O}$.

here (Fig. 4A, Table S.5; Müller et al., 2013a; Wankel et al., 2014; Goldberg, 2021). Comparing all experimental results to predicted $^{18}\alpha_{SO_2(OH)^-/H_2O(liq.)}(T)$ values leads to an RMSE of 2.2‰. However, experiments were performed at a range of pH values from $\approx$ 2 to $\approx$ 10, leading to large differences in isomer relative abundances between experimental conditions. We therefore additionally compare experimental results to predictions calculated using the

abundance-weighted average fractionation factor for all isomers at each experimental pH (assuming a 1 M solution; Eldridge et al., 2016; Millero et al., 1989). Interestingly, this leads to an RMSE of 4.5 ‰, larger than that determined when using $^{18}\alpha_{SO_2(OH)^-/H_2O(liq.)}(T)$ alone. Similar to sulfate, this result suggests that isotope exchange occurs via the hydrated isomer $SO_2(OH)^-$, as has been predicted previously (Goldberg, 2021). This hypothesis is again supported by experimentally determined oxygen isotope exchange rates, which increase with decreasing pH between ≈ 8.5 and ≈ 10.5—and thus increasing $SO_2(OH)^-$ relative abundance—following a power-law function (Betts and Voss, 1970; Wankel et al., 2014).

4.5. Aqueous sulfoxylate species

Sulfoxylate species geometries again agree closely with those calculated in Eldridge et al. (2016); bond lengths differ by a maximum of 0.02 Å and geometries differ by a maximum of 2.7° (Fig. 1; Table S.3). Like for sulfite species, there exist large differences in $^{18}\beta_{sc,AnZPE}(T)$ and $^{17}\kappa_h(T)$ between sulfoxylate isomers (Fig. 2). For example, we predict that $^{18}\alpha_{(HS)O(OH)/H_2O(liq.)}(T)$ is 21.9 ‰ higher than $^{18}\alpha_{SO_2{}^{2-}/H_2O(liq.)}(T)$ at 25 °C (Fig. 5A). Similarly, predicted $\Delta'^{17}O(T)$ for $SO_2{}^{2-}$ in equilibrium with H_2O at 25 °C is 0.046 ‰ higher than that predicted for (HS)O(OH) at the same temperature (Fig. 5B).

Interestingly, $^{18}\alpha(T)$ results for all sulfoxylate isomers either yield a crossover point [for $(HS)O_2{}^-$, $SO(OH)^-$, (HS)O(OH), and $S(OH)_2$] or predict ^{18}O depletion relative to H_2O across the entire temperature range considered [for $SO_2{}^{2-}$]. Unlike for sulfoxyanion species at all other redox states, this additionally leads to crossovers in $\Delta\Delta'^{17}O(T)$; specifically, SOO^{2-} reaches $\Delta'^{17}O(T)$ values that are 0.008 ‰ higher than that of equilibrated water at 300 °C. Because little is known about the role of sulfoxylate species in the global sulfur cycle, there exist no experimental isotope fractionation results with which we can compare our predictions. Nonetheless, seventh-order polynomial fits for calculating $^{18}\beta_{sc,AnZPE}(T)$ and $^{17}\kappa_h(T)$ values for all sulfoxylate species are reported in Tables 1–2.

4.6. Aqueous thiosulfate species

Finally, $S_2O_3{}^{2-}$ also displays a similar geometry to that calculated in Eldridge et al. (2016) (all other thiosulfate species were not included in their study); bond lengths differ by a maximum of 0.01 Å and geometries differ by a maximum of 0.4° (Fig. 1; Table S.3). Like $SO_3(OH)^-$, we additionally calculated triplicate $S_2O_2(OH)^-$ geometries and fractionation factors. Replicate geometries show similar bond lengths, with differences reaching 0.02 Å for S – O bonds, 0.03 Å for S – S and S – (OH) bonds, and 0.04 Å for O – H bonds. Bond angle differences between replicates reach 2.2° for O – S – O, 3.2° for S – O – H, 3.6° for S – S – (OH), 3.8° for S – S – O, and 5.2° for O – S – (OH). Despite these geometric differences, $^{18}\beta_{sc,AnZPE}(T)$ and $^{17}\kappa_h(T)$ are again nearly identical across replicates (Fig. 2), leading to standard deviations in $^{18}\alpha_{S_2O_2(OH)^-/H_2O(liq.)}(T)$ and $\Delta\Delta'^{17}O_{S_2O_2(OH)^-/H_2O(liq.)}(T)$ of only ±0.2 ‰ and ±0.001 ‰ at 25 °C (n = 3; Fig. 6), well within analytical precision.

Resulting $^{18}\alpha_{S_2O_3{}^{2-}/H_2O(liq.)}(T)$ and $^{18}\alpha_{S_2O_2(OH)^-/H_2O(liq.)}(T)$ predictions behave similarly to their sulfate-species counterparts; furthermore, $^{18}\alpha_{(HS)SO_3{}^-/H_2O(liq.)}(T)$ is nearly identical to $^{18}\alpha_{S_2O_2(OH)^-/H_2O(liq.)}(T)$ across all temperatures

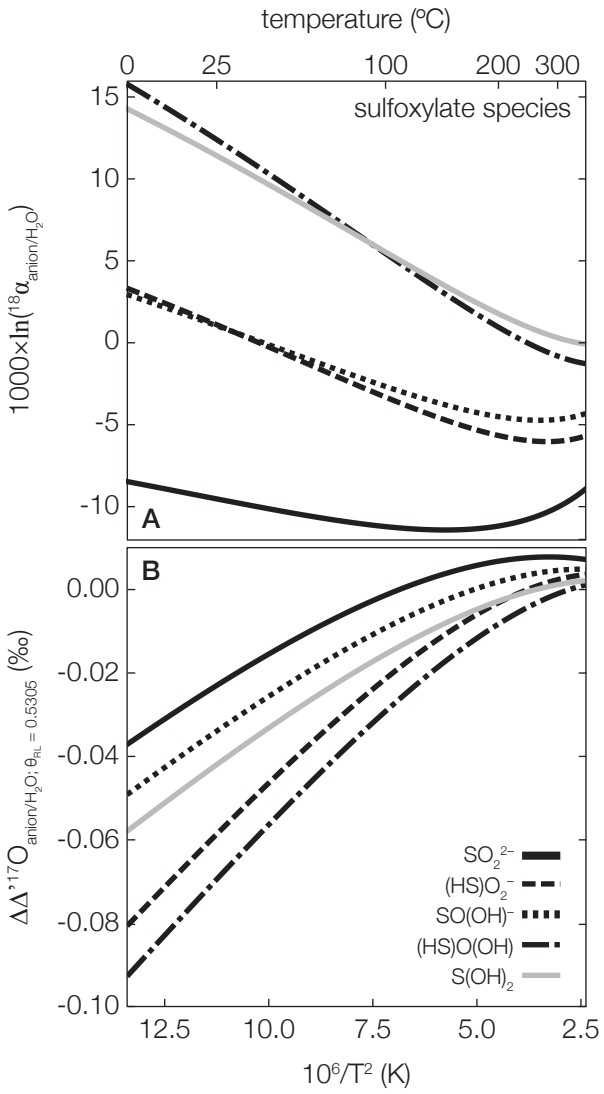

Figure 5: **Triple-oxygen fractionation factors between liquid water and sulfoxylate species.** Predicted (**A**) $1000 \times \ln(^{18}\alpha)(T)$ and (**B**) $\Delta\Delta'^{17}\mathrm{O}(T)$ between each sulfoxylate species [$SO_2{}^{2-}$, $(HS)O_2{}^-$, $SO(OH)^-$, (HS)O(OH), and $S(OH)_2$] and "semi empirical" liquid water using $^{18}\beta_{\mathrm{sc,AnZPE}}(T)$ and $^{17}\kappa_{\mathrm{h}}(T)$ values calculated by Tables 1-2. Panel (**B**) values correspond to $^{17}\theta_{\mathrm{RL}} = 0.5305$ in the definition of $\Delta'^{17}\mathrm{O}$.

(Fig. 6A). For example at 25 °C, we predict $^{18}\alpha_{S_2O_3{}^{2-}/H_2O(liq.)}(T)$ and $^{18}\alpha_{S_2O_2(OH)^-/H_2O(liq.)}(T)$ values of 22.7 ‰ and 24.7 ‰, compared to 23.3 ‰ and 27.6 ‰ for $^{18}\alpha_{SO_4{}^{2-}/H_2O(liq.)}(T)$ and $^{18}\alpha_{SO_3(OH)^-/H_2O(liq.)}(T)$. This similarity between thiosulfate- and sulfate-species fractionations additionally extends to $\Delta\Delta'^{17}\mathrm{O}(T)$ predictions (Fig. 6B). For example at 25 °C, we estimate $\Delta\Delta'^{17}\mathrm{O}_{S_2O_3{}^{2-}/H_2O(liq.)}(T)$ and $\Delta\Delta'^{17}\mathrm{O}_{S_2O_2(OH)^-/H_2O(liq.)}(T)$ values of −0.124 ‰ and −0.118 ‰, whereas predicted $\Delta\Delta'^{17}\mathrm{O}_{SO_4{}^{2-}/H_2O(liq.)}(T)$ and $\Delta\Delta'^{17}\mathrm{O}_{SO_3(OH)^-/H_2O(liq.)}(T)$ values are −0.121 ‰ and −0.128 ‰. Overall, this close agreement between isotope fractionation for sulfate and thiosulfate species likely results from the fact

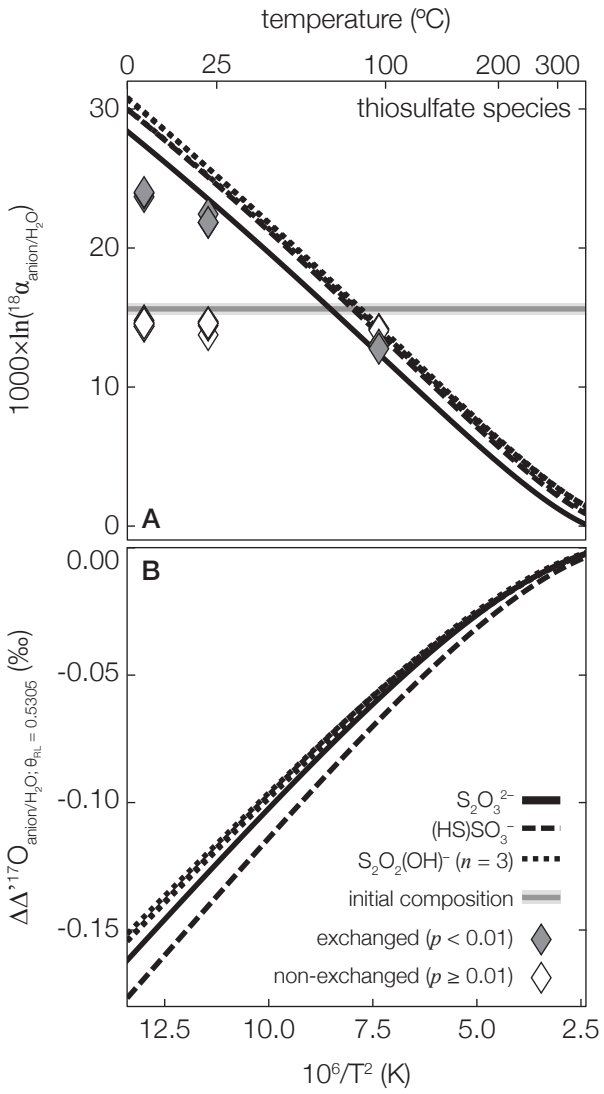

Figure 6: **Triple-oxygen fractionation factors between liquid water and thiosulfate species.** Predicted (**A**) $1000 \times \ln(^{18}\alpha)(T)$ and (**B**) $\Delta\Delta'^{17}\mathrm{O}(T)$ between each thiosulfate species [$S_2O_3^{2-}$; $(HS)SO_3^-$; and $S_2O_2(OH)^-$, $n = 3$ replicates] and "semi empirical" liquid water using $^{18}\beta_{\mathrm{sc,AnZPE}}(T)$ and $^{17}\kappa_{\mathrm{h}}(T)$ values calculated by Tables 1-2. Panel (**B**) values correspond to $^{17}\theta_{\mathrm{RL}} = 0.5305$ in the definition of $\Delta'^{17}\mathrm{O}$. Also shown in panel (**A**): experimental results for dissolved thiosulfate over a range of temperature and pH conditions (Goldberg, 2021). White diamonds indicate experiments whose $^{18}\mathrm{O}$ composition was statistically identical before and after experimental treatment, implying no oxygen-isotope exchange. Gray diamonds indicate experiments whose final $^{18}\mathrm{O}$ composition was statistically different from the starting composition, indicating isotope exchange.

519 that oxygen exchange occurs at the S(+V) sulfonate atom, rather than the S(-I) sulfonyl atom (Pryor and Tonellato,
520 1967).

Few reliable experimental equilibrium exchange fractionation factor estimates exist for thiosulfate species. We compare our predictions to recent experimental results from Goldberg (2021); however, it is likely that oxygen isotope equilibrium was not reached under some experimental conditions. We therefore exclude from our comparison any experimental results that are statistically identical to the $Na_2S_2O_3$ starting material $\delta^{18}O$ value ($p < 0.01$; two-tailed t test; Table S.5). This leads to an RMSE between our predictions and retained experimental data of 2.3 ‰ when comparing to ${}^{18}\alpha_{S_2O_3^{2-}/H_2O(liq.)}(T)$, 3.5 ‰ when comparing to ${}^{18}\alpha_{(HS)SO_3^-/H_2O(liq.)}(T)$, and 3.9 ‰ when comparing to ${}^{18}\alpha_{S_2O_2(OH)^-/H_2O(liq.)}(T)$. Interestingly, unlike for sulfate and sulfite species, thiosulfate RMSE is highest when comparing to the $S_2O_2(OH)^-$ isomer. However, this RMSE should be considered a maximum estimate since it remains possible that isotope exchange remained incomplete in these experiments. Like all other sulfoxyanion species, no experimental $\Delta\Delta'^{17}O(T)$ data exist with which we can compare our theoretical results.

5. Discussion and implications

We discuss how these equilibrium fractionation factors update our understanding of several sulfur-cycle processes—including pyrite oxidation, MSR, thiosulfate disproportionation, and hydrothermal anhydrite precipitation—that represent the major sulfur fluxes on Earth's surface. For each process, we assess whether equilibrium predictions support or refute a certain mechanistic pathway. We focus specifically on the possible incorporation of atmospheric O_2 into sulfate, as this has been previously invoked to explain fluvial and marine sulfate $\Delta'^{17}O$ values (e.g., Bao et al., 2008; Crockford et al., 2018; Killingsworth et al., 2018; Crockford et al., 2019).

5.1. Pyrite oxidation

Sulfate dissolved in modern rivers and preserved in ancient mineral deposits often displays negative $\Delta'^{17}O$ values (see Crockford et al., 2019, for compilation). This result is canonically interpreted to reflect incorporation of oxygen sourced from a mixture of water and dissolved O_2—which carries a negative mass-independent ^{17}O signal (Thiemens and Lin, 2021)—into sulfate during pyrite oxidation (Fig. 7A; e.g., Bao et al., 2008; Crockford et al., 2018; Killingsworth et al., 2018). However, dissolved sulfate in rivers draining pyrite-rich lithologies has recently been shown to exhibit $\Delta'^{17}O$ values equal to or slightly higher than those of concomitant water, questioning this mechanistic interpretation (Hemingway et al., 2020).

While several aspects of the pyrite oxidation mechanism remain unknown or underconstrained (e.g., Schoonen et al., 2010), it is generally accepted that pyrite sulfur is oxidized via a multi-step electron transfer process (the so-called "semi-conductor" model; Williamson and Rimstidt, 1994). Accordingly, pyrite sulfur acts as an anode that iteratively donates electrons to cathodic iron atoms. Electropositive sulfur is subsequently subject to nucleophilic attack by H_2O or OH^-, forming sulfoxy species and releasing H^+ to solution. Direct O_2 incorporation into sulfate is thus inconsistent with the semi-conductor model, although the importance of alternative, isotopically unique nucleophiles such as H_2O_2 remains unknown (Schoonen et al., 2010; Hemingway et al., 2020).

Here, we instead hypothesize that dissolved sulfate $\delta^{18}O$ and $\Delta'^{17}O$ values can reflect intermediate sulfoxyanion oxygen-isotope equilibrium with water and subsequent (possibly microbially mediated) dissolved-phase oxidation, either during initial pyrite oxidation or downstream redox cycling. We test this hypothesis using recently reported triple-oxygen isotope values for a time-series of Mississippi River sulfate collected at Baton Rouge, Louisiana, USA (Killingsworth et al., 2018). Pyrite oxidation-derived sulfur is released to solution either as sulfite, thiosulfate, or sulfate depending on pH (Rimstidt and Vaughan, 2003; Goldberg, 2021). Furthermore, pyrite surfaces have been shown to catalyze thiosulfate oxidation to sulfite (Xu and Schoonen, 1995), which exhibits rapid oxygen-isotope exchange under circumneutral to acidic pH values (Betts and Voss, 1970; Wankel et al., 2014). If we assume the final oxygen atom is derived from water with a negligible kinetic isotope effect (c.f., Müller et al., 2013b; Cao and Bao, 2021), then Mississippi River sulfate isotope compositions can be explained by sulfite-water equilibrium isotope exchange followed by terminal oxidation to sulfate (Fig. 7B). In contrast, these data are not consistent with a terminal oxygen atom derived from dissolved O_2 nor with thiosulfate isotope equilibrium followed by disproportionation (Fig. 7B), implicating sulfite as the critical intermediate sulfoxyanion.

Still, large uncertainties persist. For example, Goldberg (2021) showed that up to ≈40 % of released S occurs as thiosulfate in circumneutral to alkaline aerobic and anaerobic pyrite oxidation experiments, even after several weeks. Similarly, Hemingway et al. (2020) showed that pyrite oxidation-derived sulfate can retain anomalously positive $\Delta'^{17}O$ values—presumably sourced from atmospheric H_2O_2—although this signal is overprinted by downstream processes (e.g., biogeochemical sulfate recycling). In contrast, Cao and Bao (2021) reinterpreted positive $\Delta'^{17}O$ values in riverine sulfate as reflecting kinetic isotope fractionation rather than H_2O_2 incorporation, although this interpretation relies on knowledge of kinetic triple-oxygen isotope fractionation factors, which remain unconstrained. Finally, the mechanism proposed here cannot explain $\Delta'^{17}O$ values as low as -1.0 ‰ observed in Neoproterozoic sulfate deposits (Bao et al., 2008). Future laboratory- and field-based work is therefore crucial to constrain *in situ* environmental parameters such as pH, thiosulfate and sulfite concentrations and isotope compositions, and H_2O_2 concentrations at the site of pyrite oxidation.

5.2. Microbial sulfate reduction

Whereas pyrite oxidation is the dominant source of sulfate to Earth's surface, MSR and subsequent pyrite formation in marine sediments represents the dominant sink. For the purpose of tracing oxygen isotopes, MSR can be interpreted as following the simplified intracellular reaction network:

$$SO_4^{2-} \rightleftharpoons \text{APS} \rightleftharpoons SO_3^{2-} \rightleftharpoons H_2O, \tag{15}$$

where APS refers to the adenosine phosphosulfate enzyme complex; we exclude terminal reduction of SO_3^{2-} to H_2S since this does not involve oxygen exchange (Zeebe, 2010; Wankel et al., 2014; Wing and Halevy, 2014; Bertran et al., 2020). Furthermore, the oxidative back-reaction from APS to SO_4^{2-} can occur either enzymatically or abiotically (Bertran et al., 2020; Benkovic and Hevey, 1970). In the enzymatic case, sulfate is released via nulcleophilic attack

on the APS phosphorus atom; one of four oxygen atoms in resulting sulfate is thus derived from the phosphate group of adenosine monophosphate (AMP; Brunner et al., 2012). In the abiotic case however, sulfate is nearly quantitatively released by a unimolecular elimination reaction, leading to sulfate with three oxygen atoms derived from sulfite and one oxygen atom directly sourced from water (Benkovic and Hevey, 1970). At Earth-surface conditions, neither sulfate nor APS are known to exchange oxygen atoms with ambient water (Chiba and Sakai, 1985; Kohl et al., 2012), implicating sulfite and AMP phosphate as the primary species by which oxygen-isotope exchange can occur.

Depending on thermodynamic conditions and substrate concentrations—and thus sulfate reduction rates—MSR will exist between purely kinetic (i.e., unidirectional forward fluxes in Eq. 15) and equilibrium (i.e., equal forward and backward fluxes in Eq. 15) limits (Wing and Halevy, 2014). At the kinetic limit, all generated SO_3^{2-} is completely reduced to H_2S within the cell; at the equilibrium limit however, isotopically equilibrated SO_3^{2-} can back-react to SO_4^{2-}. The exact position between these limits therefore determines the degree to which equilibrium isotope exchange during MSR (including AMP phosphate-derived oxygen for the enzymatic oxidation reaction) impacts marine sulfate oxygen isotope compositions (Bertran et al., 2020). Using a thermodynamic model, Wing and Halevy (2014) estimated that MSR in marine sediments likely approaches the equilibrium limit, even in coastal regions with high sulfate reduction rates. This has since been confirmed in several field localities by tracking porewater sulfate ^{33}S and ^{34}S evolution with sediment depth; results are inconsistent with MSR operating in the kinetic regime (Masterson et al., 2018, 2021). Several aspects of equilibrium oxygen isotope exchange during MSR remain unknown or underconstrained, particularly regarding the timescale of AMP phosphate oxygen exchange (Brunner et al., 2012; Chang and Blake, 2015). Nevertheless, here we use our theoretical predictions to estimate two end-member scenarios that may prove useful for interpreting field results:

(i) Full expression of the sulfate-water equilibrium fractionation factor. At the equilibrium limit, Bertran et al. (2020) estimated that the abiotic elimination pathway likely dominates the oxidative APS back-reaction. If true, this implies that SO_4^{2-} regeneration involves an activated transition state resembling $\mathrm{AMP}\cdots\mathrm{SO_3}\cdots\mathrm{H_2O}$, which may rapidly exchange oxygen atoms with water (Benkovic and Hevey, 1970). Such a direct sulfate-water exchange mechanism has been invoked previously to explain the similarity between observed and theoretical sulfate $\delta^{18}O$ predictions (Zeebe, 2010); however, this similarity may be fortuitous rather than mechanistic (Brunner et al., 2012). It additionally remains unclear whether the expressed isotope effect should reflect SO_4^{2-}—the isomer released by oxidative back-reaction—or $SO_3(OH)^-$—as would be the case for direct, abiotic oxygen exchange (Fig. 3A). In either case, our results predict direct sulfate-water equilibrium during MSR would push sulfate to higher $\delta^{18}O$ and lower $\Delta'^{17}O$ with a ${}^{17}\theta_{SO_4^{2-}/H_2O}(T)$ value ranging from 0.5250 to 0.5253 between 0 and 25 °C [or 0.5255 to 0.5258 if using ${}^{17}\theta_{SO_3(OH)^-/H_2O}(T)$]. For the modern ocean, this equates to an equilibrium MSR sulfate composition with $\delta^{18}O$ ranging from 23.3 to 28.9 ‰ and $\Delta'^{17}O$ ranging from −0.120 to −0.159 ‰ between 0 and 25 °C [or $\delta^{18}O$ from 27.6 to 33.4 ‰ and $\Delta'^{17}O$ from −0.167 to −0.129 ‰ if using $SO_3(OH)^-$].

(ii) A weighted-average of the sulfite-water (75 %) and AMP phosphate-water (25 %) equilibrium fractionation factors. If we assume that the residence times of sulfite and AMP phosphate are long enough such that both reach

isotopic equilibrium with water, the overall expressed sulfate-water fractionation should represent a weighted average of these two species (Brunner et al., 2012). Here, we ignore any additional fractionation between SO_3^{2-} and APS and between APS and SO_4^{2-} since their triple-oxygen fractionation factors remain unknown, although these steps may prove important. Unfortunately, AMP phosphate triple-oxygen isotope fractionation factors have also not been measured or theoretically predicted. We instead use theoretical fluoroapatite predictions from Schauble and Young (2021); these are in close agreement with experimentally derived dissolved phosphate ^{18}O fractionations and should thus serve as a useful first approximation (Chang and Blake, 2015). Assuming sulfite fractionation occurs via $SO_2(OH)^-$ rather than SO_3^{2-} *sensu stricto* (Fig. 4), this results in an expressed $^{17}\theta(T)$ ranging from 0.5237 to 0.5240 for temperatures between 0 and 25 °C. For the modern ocean, this leads to equilibrium MSR-derived sulfate $\delta^{18}O$ ranging from 13.0 ‰ to 16.9 ‰ and $\Delta'^{17}O$ ranging from −0.086 ‰ to −0.114 ‰. However, these $\delta^{18}O$ values are ≈10 ‰ lower than porewater observations, suggesting additional fractionation during reoxidation back-reactions (Zeebe, 2010; Brunner et al., 2012).

Waldeck et al. (2019) recently reported that marine sulfate is described by $\delta^{18}O$ and $\Delta'^{17}O$ values of 8.67 ± 0.21 ‰ and −0.016 ± 0.017 ‰, respectively. For both scenarios described here, this is consistent with a mixture between MSR recycling and an ^{18}O-depleted, ^{17}O-enriched input, presumably dissolved riverine sulfate (Hemingway et al., 2020). Although several aspects of MSR triple-oxygen isotope fractionation remain underconstrained, one common feature of all predictions derived here is the generation of sulfate with $\Delta'^{17}O$ values lower than those of ambient water. It thus becomes clear that observed slightly negative $\Delta'^{17}O$ values of fluvial and marine sulfate (Killingsworth et al., 2018; Waldeck et al., 2019) can be explained purely by sulfate-water equilibrium during MSR operating near the equilibrium limit without the need to invoke incorporation of anomalously ^{17}O-depleted dissolved O_2.

5.3. Thiosulfate disproportionation

Thiosulfate is produced by the partial oxidation of sulfide at redox boundaries, for example when aerated water penetrates into anoxic hot springs (Xu et al., 1998) or marine sediments (Jørgensen, 1990). At circumneutral pH, $S_2O_2(OH)^-$ isotopically exchanges oxygen with surrounding water with a half life on the order of hours (the presence of $SO_2(OH)^-$ can also act as a minor catalyst for this exchange; Pryor and Tonellato, 1967). Thiosulfate can then disproportionate either biologically or abiotically, but these two mechanisms follow unique reaction pathways. Microbial thiosulfate disproportionation has been shown to proceed as (Jørgensen, 1990; Finster et al., 1998):

$$S_2O_3^{2-} + H_2O \longrightarrow SO_4^{2-} + HS^- + H^+. \tag{16}$$

In contrast, abiotic disproportionation is thought to involve a suite of reactions with the rate-limiting step described by the bimolecular reaction (Johnston and McAmish, 1973; Xu and Schoonen, 1995; Xu et al., 1998):

$$S_2O_2(OH)^- + S_2O_3^{2-} \longrightarrow S_2 + SO_2(OH)^- + SO_3^{2-}. \tag{17}$$

Assuming (i) reactant $S_2O_3^{2-}$ reaches isotopic equilibrium with water, (ii) microbial disproportionation proceeds unidirectionally (i.e., no back-reaction in Eq. 16), and (iii) the final oxygen atom is derived from water with a

negligible kinetic isotope effect (c.f., Cao and Bao, 2021), then microbial disproportionation will yield product sulfate with $\delta^{18}O$ and $\Delta'^{17}O$ values $\approx$20 ‰ higher and $\approx$0.15 ‰ lower than surrounding water, respectively (Fig. 7C). While each of these assumptions must be thoroughly validated (e.g., the residence time of thiosulfate in a given environment may be too short to reach isotopic equilibrium), this calculation nevertheless provides a useful end-member scenario to interpret environmental data.

In contrast, abiotic thiosulfate disproportionation produces sulfite, which will itself rapidly exchange oxygen isotopes with surrounding water (Fig. 7B). The original thiosulfate isotope signature is therefore overprinted by sulfite oxygen exchange, independent of the degree to which reactant thiosulfate and water reached isotope equilibrium. Subsequent oxidation will yield sulfate with an isotope signature that reflects a mixing between equilibrated sulfite and the final oxygen atom source (in addition to any kinetic effects; Cao and Bao, 2021).

5.4. Hydrothermal oxygen isotope exchange

Finally, we briefly consider hydrothermal oxygen-isotope exchange between water and sulfate. Although exchange is negligible at Earth-surface conditions—even over billion-year timescales—exchange rates increase drastically at elevated temperatures characteristic of hydrothermal vents (Chiba and Sakai, 1985). Measured $\delta^{18}O$ values of laboratory hydrothermally precipitated anhydrite ($CaSO_4$) are consistent with our $SO_3(OH)^-$ fractionation predictions (Fig. 2A), supporting equilibrium exchange under these conditions (Lloyd, 1968; Chiba et al., 1981). However, no hydrothermal anhydrite $\Delta'^{17}O$ records currently exist to our knowledge. Nevertheless, anhydrite $\delta^{18}O$ has been used as a proxy for alteration fluid temperature at the time of mineral precipitation, although this requires that alteration fluid oxygen-isotope composition is accurately known (e.g., Teagle et al., 1998) and that anhydrite-water equilibrium is reached in natural vent settings (c.f., Chiba et al., 1998). Still, if the temperature of isotope exchange can be constrained independently (e.g., by traditional or "clumped" isotope thermometry of co-existing carbonates; Weinzierl et al., 2018) and equilibrium exchange can be ensured (e.g., by additionally measuring $\delta^{34}S$; Chiba et al., 1998), then hydrothermal anhydrite veins preserved in oceanic crust and obducted ophiolites may record the triple-oxygen isotope composition of alteration fluid in the geologic past. This hypothesis remains speculative but warrants further study.

6. Conclusions

The triple-oxygen isotope composition of sulfate ($\delta^{18}O$ and $\Delta'^{17}O$)—both in modern aquatic systems and in geologically preserved sulfate-bearing minerals—is becoming a common tool to constrain sulfur-cycle processes. However, equilibrium oxygen-isotope fractionation factors between water and intermediate sulfoxyanion species remain largely unknown. Here, we estimate fractionation factors for a suite of sulfoxyanions—including several protonated isomers—using a quantum-chemistry computational approach; our results are in good agreement with all available experimental constraints. We highlight the potential importance of short-lived thiosulfate and, especially, sulfite species in setting $\delta^{18}O$ and $\Delta'^{17}O$ values of sulfate produced by several abiotic and biological processes (e.g., pyrite

oxidation, MSR, thiosulfate disproportionation, anhydrite precipitation). Importantly, when equilibrium sulfite or thiosulfate fractionation factors are expressed, resulting sulfate can exhibit $\Delta'^{17}O$ values up to $\approx 0.16‰$ lower than equilibrated water. Slightly negative $\Delta'^{17}O$ values thus do not require incorporation of alternative oxygen sources such as dissolved O_2, as has been previously assumed. This result carries implications for the interpretation of isotope signals recorded in geologic sulfate archives.

Declaration of competing interests

The authors declare that they have no known competing financial interests or personal relationships that could have appeared to influence the work reported in this paper.

Acknowledgements

The computations in this paper were run on the FASRC Cannon cluster supported by the FAS Division of Science Research Computing Group at Harvard University. This result is part of a project that has received funding from the European Research Council (ERC) under the European Union's Horizon 2020 research and innovation program (Grant agreement No. 946150, to J.D.H.). Additional funding was provided by the American Chemical Society Petroleum Research Fund (Grant No. 59455-ND2, to J.D.H. and D.T.J.). We thank Nir Galili, Itay Halevy, and Cornelia Mertens for helpful discussions.

Research Data

Research data associated with this article (including all optimization and frequency output files, derived quantities, and Python scripts used to generate derived quantities) can be accessed in the Supplementary Data and Tables S.1–S.4.

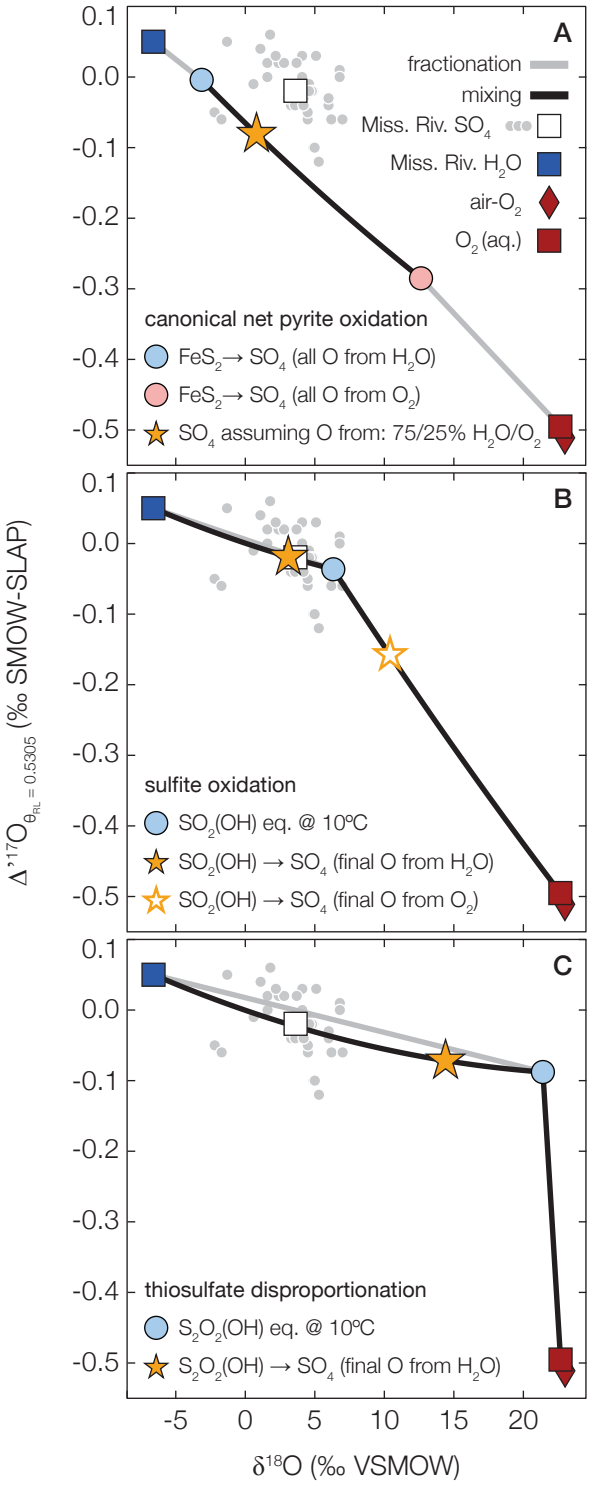

Figure 7: Caption on following page.

Figure 7: **New and canonical interpretations of sulfate isotope compositions in the oxidative sulfur cycle.** Predicted sulfate triple-oxygen isotope compositions following: (**A**) canonical interpretations of experimentally observed net pyrite oxidation isotope effects, (**B**) sulfite-water isotope equilibrium at 10 °C followed by oxidation to sulfate, (**C**) thiosulfate-water isotope equilibrium at 10 °C followed by disproportionation to sulfate and hydrogen sulfide (Eq. 16). Mississippi River dissolved sulfate isotope compositions are used as an example dataset to test these predictions. Markers common to all panels are as follows: blue squares = average Mississippi River water at Arkansas City, AR, USA (1984–1987; n = 10; Coplen and Kendall, 2000; Killingsworth et al., 2018); red diamonds = atmospheric O_2 (Sharp and Wostbrock, 2021); red squares = dissolved oxygen in equilibrium with atmospheric O_2 at 10 °C (Benson and Krause, 1984; Luz and Barkan, 2009); gray circles = individual Mississippi River dissolved sulfate samples (2009–2014, n = 38; Killingsworth et al., 2018); white squares = Mississippi River dissolved sulfate average composition; gray lines = fractionation trajectories; black lines = mixing trajectories. Originally reported Mississippi River sulfate $\Delta'^{17}O$ values have been shifted up by 0.07 ‰ as recommended by Cao and Bao (2021) to place results closer to the SMOW–SLAP calibration scale. For panel (**A**), $^{18}\alpha(T)$ values of net pyrite oxidation with all O from either H_2O or O_2 are taken from Balci et al. (2007); corresponding $\Delta\Delta'^{17}O(T)$ values have not been measured and are assumed here to follow kinetic fractionation lines with slopes defined by the reduced masses of reactants (c.f., Cao and Bao, 2021, their Table 1). We assume final sulfate contains 75 % O from H_2O and 25 % O from O_2, consistent with previous interpretations (Balci et al., 2007; Kohl and Bao, 2011). For panels (**B**) and (**C**), we assume equilibrium fractionations are set by the $-$OH protonated isomer (see main text) and that sulfite/thiosulfate is quantitatively oxidized/disproportionated such that any kinetic fractionation is not expressed; fractionation of H_2O during oxidation/disproportionation is not constrained but is thought to be of minor importance (c.f., Müller et al., 2013b). All $\Delta'^{17}O$ values correspond to $^{17}\theta_{RL}$ = 0.5305 and are reported on the SMOW–SLAP calibration scale whenever possible (Sharp and Wostbrock, 2021). Importantly, only sulfite equilibrium followed by oxidation with terminal oxygen from H_2O can explain observed Mississippi River results.

Table 1: Seventh-order polynomial fit parameters to the equation: $\ln\left({}^{18}\beta_{sc,AnZPE}\right) = \sum \frac{p[i]}{T^i}$, where T is in Kelvin. n.a. = not applicable; RMSE = root mean square error between "true" values and polynomial fits; redox = sulfur atom redox state.

compound	redox	solvation	p[7]	p[6]	p[5]	p[4]	p[3]	p[2]	p[1]	p[0]	RMSE
SO_4^{2-}	S(+VI)	$30 \cdot H_2O$	6.71983E+14	-1.61853E+13	1.55800E+11	-6.92010E+08	4.71107E+05	1.07129E+04	-6.34245E-02	-4.31412E-05	1.18249E-08
[a]$SO_3(OH)^-$	S(+VI)	$30 \cdot H_2O$	6.42758E+14	-1.44847E+13	1.26996E+11	-4.59340E+08	-5.26527E+05	1.27540E+04	-2.25825E-01	-2.55063E-05	1.52270E-08
SO_3^{2-}	S(+IV)	$30 \cdot H_2O$	9.65722E+13	-4.72757E+12	6.41338E+10	-3.50424E+08	1.80059E+05	8.37455E+03	-8.17461E-02	-2.33992E-05	9.66507E-09
$(HS)O_3^-$	S(+IV)	$30 \cdot H_2O$	1.19753E+15	-2.58780E+13	2.26145E+11	-9.21568E+08	6.82041E+05	1.07448E+04	7.50802E-02	-5.29071E-05	1.05068E-08
$SO_2(OH)^-$	S(+IV)	$30 \cdot H_2O$	-1.42207E+15	2.25286E+13	-1.47577E+11	5.86347E+08	-2.38605E+06	1.24401E+04	-7.26147E-01	6.83000E-05	4.36272E-08
$SO_{2(aq.)}$	S(+IV)	$30 \cdot H_2O$	2.09996E+15	-4.14976E+13	3.31216E+11	-1.23237E+09	9.16717E+05	1.07171E+04	1.35312E-01	-5.86532E-05	7.36303E-09
SO_2^{2-}	S(+II)	$30 \cdot H_2O$	-7.83473E+13	-2.55820E+11	1.96245E+10	-1.47042E+08	-6.08026E+04	6.90117E+03	-1.42854E-01	-4.15583E-06	5.63571E-09
$(HS)O_2^-$	S(+II)	$30 \cdot H_2O$	2.41201E+14	-7.71323E+12	8.83390E+10	-4.38100E+08	2.81597E+05	8.15697E+03	-1.83875E-02	-2.89196E-05	1.02254E-08
$SO(OH)^-$	S(+II)	$30 \cdot H_2O$	-3.04105E+15	5.15672E+13	-3.66460E+11	1.45436E+09	-4.08682E+06	1.27793E+04	-7.57725E-01	3.86768E-05	8.94471E-08
(HS)O(OH)	S(+II)	$30 \cdot H_2O$	-1.70790E+15	2.87171E+13	-2.05392E+11	8.90214E+08	-3.33834E+06	1.39637E+04	-1.11214E+00	1.44934E-04	3.81857E-08
$S(OH)_2$	S(+II)	$30 \cdot H_2O$	-5.32562E+15	9.34092E+13	-6.94394E+11	2.88493E+09	-7.84381E+06	1.85433E+04	-1.77959E+00	1.92174E-04	1.27278E-07
$S_2O_3^{2-}$	S(-I)/S(+V)	$30 \cdot H_2O$	9.02941E+14	-2.04082E+13	1.86022E+11	-7.89124E+08	5.70025E+05	1.06998E+04	-1.53035E-02	-4.78065E-05	1.11113E-08
$(HS)SO_3^-$	S(-I)/S(+V)	$30 \cdot H_2O$	1.34299E+15	-2.82213E+13	2.40665E+11	-9.61873E+08	7.10344E+05	1.10419E+04	1.30072E-02	-5.20276E-05	8.62323E-09
[a]$S_2O_2(OH)^-$	S(-I)/S(+V)	$30 \cdot H_2O$	5.51092E+14	-1.13581E+13	9.14132E+10	-2.68095E+08	-1.01514E+06	1.30976E+04	-6.98263E-01	8.58174E-05	1.01536E-08
$O_{2(aq.)}$	n.a.	$30 \cdot H_2O$	5.63583E+15	-9.44188E+13	6.18801E+11	-1.76461E+09	2.34067E+05	1.27826E+04	-7.54232E-01	1.05164E-04	1.02871E-07
$O_{2(g)}$	n.a.	$0 \cdot H_2O$	6.31165E+15	-1.03614E+14	6.59604E+11	-1.77690E+09	-2.20903E+05	1.38854E+04	-9.69969E-01	1.75577E-04	1.35002E-07
[b]$H_2O_{(liq.)}$	n.a.	$30 \cdot H_2O$	-2.08862E+15	4.25765E+13	-3.75879E+11	1.88200E+09	-5.91132E+06	1.29812E+04	7.52028E+00	-2.95070E-03	7.64788E-09
[c]$H_2O_{(liq.)}$	n.a.	$30 \cdot H_2O$	-1.43935E+15	2.94746E+13	-2.63299E+11	1.34665E+09	-3.98119E+06	7.27847E+03	1.77318E+01	-1.14770E-02	6.18469E-09
[d]$H_2O_{(liq.)}$	n.a.	$30 \cdot H_2O$	-3.4595E+16	6.90085E+14	-5.90267E+12	2.81504E+10	-8.08683E+07	1.41111E+05	-1.14205E+02	4.60253E-02	1.46264E-07
$H_2O_{(vap.)}$	n.a.	$0 \cdot H_2O$	-1.26969E+16	2.18888E+14	-1.60102E+12	6.48294E+09	-1.59050E+07	2.42446E+04	2.18983E-02	-4.74044E-04	4.59327E-07

[a] average of repeat optimizations (n = 3).

[b] calculated for 0 °C ≤ T ≤ 375 °C.

[c] freshwater; semi-empirical using ${}^{18}\alpha_{liq./vap.}(T)$ from Horita et al. (2008) (their Eq. 20); calculated for 0 °C ≤ T ≤ 375 °C.

[d] 4 M NaCl; semi-empirical semi-empirical using ${}^{18}\alpha_{liq./vap.}(T)$ from Horita et al. (1995) (their Eq. 10); calculated for 0 °C ≤ T ≤ 375 °C.

Table 2: Seventh-order polynomial fit parameters to the equation: $^{17}\kappa_h = \sum \frac{p[i]}{T^i}$, where T is in Kelvin. n.a. = not applicable; RMSE = root mean square error between "true" values and polynomial fits; redox = sulfur atom redox state.

compound	redox	solvation	p[7]	p[6]	p[5]	p[4]	p[3]	p[2]	p[1]	p[0]	RMSE
SO_4^{2-}	S(+VI)	$30 \cdot H_2O$	-1.57179E+14	3.02584E+12	-2.41713E+10	9.68043E+07	-1.59320E+05	-9.83867E+01	-3.94720E-02	5.30424E-01	1.77841E-09
[a]$SO_3(OH)^-$	S(+VI)	$30 \cdot H_2O$	-3.63256E+13	8.95203E+11	-8.12914E+09	3.00902E+07	9.52242E+02	-2.87611E+02	-1.93408E-02	5.30526E-01	1.89045E-09
SO_3^{2-}	S(+IV)	$30 \cdot H_2O$	4.05119E+12	1.23347E+11	-2.59095E+09	1.45034E+07	-4.54892E+03	-1.93426E+02	-7.79176E-03	5.30511E-01	9.96271E-10
$(HS)O_3^-$	S(+IV)	$30 \cdot H_2O$	-8.29003E+13	1.77492E+12	-1.49888E+10	5.70005E+07	-4.72955E+04	-2.70009E+02	-1.95176E-02	5.30525E-01	9.06552E-10
$SO_2(OH)^-$	S(+IV)	$30 \cdot H_2O$	1.42687E+14	-2.24365E+12	1.44854E+10	-5.30482E+07	1.50432E+05	-3.71653E+02	2.10520E-02	5.30546E-01	5.02504E-09
$SO_{2(aq.)}$	S(+IV)	$30 \cdot H_2O$	-1.70746E+14	3.34525E+12	-2.60128E+10	9.20869E+07	-7.98336E+04	-3.20578E+02	-2.87601E-02	5.30520E-01	7.11728E-10
SO_2^{2-}	S(+II)	$30 \cdot H_2O$	1.36083E+13	-1.28806E+11	-1.40008E+08	4.15153E+06	6.81817E+03	-1.59082E+02	-2.61210E-03	5.30530E-01	6.84546E-10
$(HS)O_2^-$	S(+II)	$30 \cdot H_2O$	-2.72978E+13	6.91624E+11	-6.88155E+09	3.10983E+07	-3.51355E+04	-1.75851E+02	-1.00567E-02	5.30493E-01	2.21929E-10
$SO(OH)^-$	S(+II)	$30 \cdot H_2O$	2.48261E+14	-4.01989E+12	2.65893E+10	-9.29062E+07	1.98452E+05	-3.23404E+02	-9.71134E-03	5.30547E-01	9.54517E-09
(HS)O(OH)	S(+II)	$30 \cdot H_2O$	1.53216E+14	-2.48438E+12	1.66017E+10	-6.18736E+07	1.66250E+05	-3.73351E+02	3.40398E-02	5.30493E-01	4.37789E-09
$S(OH)_2$	S(+II)	$30 \cdot H_2O$	4.13506E+14	-6.89874E+12	4.74673E+10	-1.72543E+08	3.59358E+05	-4.60714E+02	2.07488E-02	5.30489E-01	1.34962E-08
$S_2O_3^{2-}$	S(-I)/S(+V)	$30 \cdot H_2O$	-6.80459E+13	1.48581E+12	-1.28759E+10	5.08838E+07	-4.82633E+04	-2.41047E+02	-1.72485E-02	5.30504E-01	6.23001E-10
$(HS)SO_3^-$	S(-I)/S(+V)	$30 \cdot H_2O$	-8.46801E+13	1.80113E+12	-1.50780E+10	5.64704E+07	-4.22162E+04	-2.85061E+02	-1.91377E-02	5.30532E-01	9.97833E-10
[a]$S_2O_2(OH)^-$	S(-I)/S(+V)	$30 \cdot H_2O$	-1.70020E+13	4.64197E+11	-4.29933E+09	1.29925E+07	3.94303E+04	-3.25886E+02	1.46467E-02	5.30509E-01	4.68220E-10
$O_{2(aq.)}$	n.a.	$30 \cdot H_2O$	-5.85116E+14	9.32641E+12	-5.63098E+10	1.36112E+08	3.71855E+04	-6.83195E+02	6.46825E-02	5.30589E-01	1.26270E-08
$O_{2(g)}$	n.a.	$0 \cdot H_2O$	-6.63197E+14	1.03607E+13	-6.07309E+10	1.37570E+08	7.75226E+04	-7.83262E+02	9.96618E-02	5.30495E-01	1.67365E-08
[b]$H_2O_{(liq.)}$	n.a.	$30 \cdot H_2O$	1.60477E+13	-1.59193E+11	-4.82941E+08	1.47080E+07	-9.66360E+04	3.28785E+02	-7.15169E-01	5.30747E-01	3.02471E-10
[c]$H_2O_{(liq.)}$	n.a.	$30 \cdot H_2O$	6.30968E+14	-1.22153E+13	1.00465E+11	-4.53691E+08	1.20386E+06	-1.83622E+03	1.31428E+00	5.29776E-01	3.47385E-09
[d]$H_2O_{(liq.)}$	n.a.	$30 \cdot H_2O$	2.26447E+14	-4.73876E+12	4.24174E+10	-2.09822E+08	6.12064E+05	-1.02664E+03	7.70880E-01	5.29884E-01	6.12940E-10
$H_2O_{(vap.)}$	n.a.	$0 \cdot H_2O$	1.60477E+13	-1.59193E+11	-4.82941E+08	1.47080E+07	-9.66360E+04	3.28785E+02	-7.15169E-01	5.30747E-01	3.02471E-10

[a] average of repeat optimizations ($n = 3$).

[b] calculated for 0 °C ≤ T ≤ 375 °C.

[c] freshwater; semi-empirical using $^{18}\alpha_{liq./vap.}(T)$ from Horita et al. (2008) (their Eq. 20); calculated for 0 °C ≤ T ≤ 375 °C.

[d] 4 M NaCl; semi-empirical semi-empirical using $^{18}\alpha_{liq./vap.}(T)$ from Horita et al. (1995) (their Eq. 10); calculated for 0 °C ≤ T ≤ 375 °C.

References

N. Balci, W. C. Shanks III, B. Mayer, and K. W. Mandernack. Oxygen and sulfur isotope systematics of sulfate produced by bacterial and abiotic oxidation of pyrite. *Geochimica et Cosmochimica Acta*, 71:3796–3811, 2007.

H. Bao, J. Lyons, and C. Zhou. Triple oxygen isotope evidence for elevated CO_2 levels after a Neoproterozoic glaciation. *Nature*, 453:504–506, 2008.

E. Barkan and B. Luz. High precision measurements of $^{17}O/^{16}O$ and $^{18}O/^{16}O$ ratios in H_2O. *Rapid Communications in Mass Spectrometry*, 19:3737–3742, 2005.

A. D. Becke. A new mixing of Hartree-Fock and local density-functional theories. *Journal of Chemical Physics*, 98: 1372–1377, 1993.

S. Benkovic and R. Hevey. Studies in sulfate esters. V. The mechanism of hydrolysis of phenyl phosphosulfate, a model system for 3'-phosphoadenosine 5'-phosphosulfate. *Journal of the American Chemical Society*, 92:4971–4977, 1970.

B. B. Benson and D. Krause, Jr. The concentration and isotopic fractionation of oxygen dissolved in freshwater and seawater in equilibrium with the atmosphere. *Limnology & Oceanography*, 29:620–632, 1984.

R. A. Berner. Sedimentary pyrite formation: an update. *Geochimica et Cosmochimica Acta*, 48:605–615, 1984.

R. A. Berner. Modeling atmospheric O_2 over Phanerozoic time. *Geochimica et Cosmochimica Acta*, 65:685–694, 2001.

E. Bertran, A. Waldeck, B. A. Wing, I. Halevy, W. D. Leavitt, A. S. Bradley, and D. T. Johnston. Oxygen isotope effects during microbial sulfate reduction: applications to sediment cell abundances. *The ISME Journal*, 14:1508–1519, 2020.

R. Betts and R. Voss. The kinetics of oxygen exchange between the sulfite ion and water. *Canadian Journal of Chemistry*, 48:2035–2041, 1970.

J. Bigeleisen and M. Goeppert Mayer. Calculation of equilibrium constants for isotopic exchange reactions. *Journal of Chemical Physics*, 15:261–267, 1947.

C. L. Blättler, M. Claire, A. Prave, K. Kirsimäe, J. A. Higgins, P. Medvedev, A. Romashkin, D. Rychanchik, A. Zerkle, K. Paiste, T. Kreitsmann, I. Miller, J. Hayles, H. Bao, A. Turchyn, M. Warke, and A. Lepland. Two-billion-year-old evaporites capture Earth's great oxidation. *Science*, 360:320–323, 2018.

M. Born and K. Huang. *Dynamical theory of crystal lattices*. Clarendon press, 1954.

M. Born and J. R. Oppenheimer. Zur quantentheorie der molekeln. *Annalen der Physik*, 389:457–484, 1927.

C. Brandt and R. van Eldik. Transition metal-catalyzed oxidation of sulfur(IV) oxides. Atmospheric-relevant processes and mechanisms. *Chemical Reviews*, 95:119–190, 1995.

B. Brunner, F. Einsiedl, G. L. Arnold, I. Müller, S. Templer, and S. M. Bernasconi. The reversibility of dissimilatory sulphate reduction and the cell-internal multi-step reduction of sulphite to sulphate: insights from the oxygen isotope composition of sulphate. *Isotopes in Environmental and Health Studies*, 48:33–54, 2012.

A. Burke, T. M. Present, G. Paris, E. C. Rae, B. H. Sandilands, J. Gaillardet, B. Peucker-Ehrenbrink, W. W. Fischer, J. W. McClelland, R. G. Spencer, B. M. Voss, and J. F. Adkins. Sulfur isotopes in rivers: insights into global weathering budgets, pyrite oxidation, and the modern sulfur cycle. *Earth and Planetary Science Letters*, 496: 168–177, 2018.

E. I. Burt, M. Bill, M. E. Conrad, A. J. C. Quispe, J. N. Christensen, R. G. Hilton, M. Dellinger, and A. J. West. Conservative transport of dissolved sulfate across the Rio Madre de Dios floodplain in Peru. *Geology*, 49:1064–1068, 2021.

X. Cao and H. Bao. Small triple oxygen isotope variations in sulfate: mechanisms and applications. *Reviews in Mineralogy & Geochemistry*, 86:463–488, 2021.

X. Cao and Y. Liu. Equilibrium mass-dependent fractionation relationships for triple oxygen isotopes. *Geochimica et Cosmochimica Acta*, 75:7435–7445, 2011.

X. Cao and Y. Liu. Theoretical estimation of the equilibrium distribution of clumped isotopes in nature. *Geochimica et Cosmochimica Acta*, 77:292–303, 2012.

S. J. Chang and R. E. Blake. Precise calibration of equilibrium oxygen isotope fractionations between dissolved phosphate and water from 3 to 37°C. *Geochimica et Cosmochimica Acta*, 150:314–329, 2015.

H. Chiba and H. Sakai. Oxygen isotope exchange rate between dissolved sulfaate and water at hydrothermal temperatures. *Geochimica et Cosmochimica Acta*, 49:993–1000, 1985.

H. Chiba, M. Kusakabe, S.-I. Hirano, S. Matsuo, and S. Shigeyuki. Oxygen isotope fractionation factors between anhydrite and water from 100 to 550°C. *Earth and Planetary Science Letters*, 53:55–62, 1981.

H. Chiba, N. Uchiyama, and D. A. Teagle. Stable isotope study of anhydrite and sulfide mienrals at the TAG hydrothermal mound, Mid-Atlantic Ridge, 26°N. In P. Herzig, S. Miller, and R. Zierenberg, editors, *Proceedings of the Ocean Drilling Program, Scientific Results*, volume 158, pages 85–90, 1998.

T. B. Coplen and C. Kendall. Stable hydrogen and oxygen isotope ratios for selected sites of the US Geological Survey's NASQAN and benchmark surface-water networks. Technical report, United States Geological Survey, 2000.

P. W. Crockford, J. A. Hayles, H. Bao, N. J. Planavsky, A. Bekker, P. W. Fralick, G. P. Halverson, T. H. Hui, Y. Peng, and B. A. Wing. Triple oxygen isotope evidence for limited mid-Proterozoic primary productivity. *Nature*, 559: 613–616, 2018.

P. W. Crockford, M. Kunzmann, A. Bekker, J. Hayles, H. Bao, G. P. Halverson, Y. Peng, T. H. Bui, G. M. Cox, T. M. Gibson, S. Wörndle, R. Rainbird, A. Lepland, N. L. Swanson-Hysell, S. Master, B. Sreenivas, A. Kuznetsov, V. Krupenik, and B. A. Wing. Claypool continued: extending the isotopic record of sedimentary sulfate. *Chemical Geology*, 513:200–225, 2019.

D. L. Eldridge, W. Guo, and J. Farquhar. Theoretical estimates of equilibrium sulfur isotope effects in aqueous sulfur systems: highlighting the role of isomers in the sulfite and sulfoxylate systems. *Geochimica et Cosmochimica Acta*, 195:171–200, 2016.

D. L. Eldridge, A. Kamyshny Jr., and J. Farquhar. Theoretical estimates of equilibrium sulfur isotope effects among aqueous polysulfur and associated compounds with applications to authigenic pyrite formation and hydrothermal disproportionation reactions. *Geochimica et Cosmochimica Acta*, 310:281–319, 2021.

D. A. Fike, A. S. Bradley, and C. V. Rose. Rethinking the ancient sulfur cycle. *Annual Reviews of Earth and Planetary Science*, 43:593–622, 2015.

K. Finster, W. Liesack, and B. Thamdrup. Elemental sulfur and thiosulfate disproportionation by *desulfocapsa sulfoexigens* sp. nov., a new anaerobic bacterium isolated from marine surface sediment. *Applied and Environmental Microbiology*, 64:119–125, 1998.

M. J. Frisch, M. Head-Gordon, and J. A. Pople. A direct MP2 gradient method. *Chemical Physics Letters*, 166: 275–280, 1990.

M. J. Frisch, G. W. Trucks, H. B. Schlegel, G. E. Scuseria, M. A. Robb, J. R. Cheeseman, G. Scalmani, V. Barone, G. A. Petersson, H. Nakatsuji, X. Li, M. Caricato, A. V. Marenich, J. Bloino, B. G. Janesko, R. Gomperts, B. Mennucci, H. P. Hratchian, J. V. Ortiz, A. F. Izmaylov, J. L. Sonnenberg, D. Williams-Young, F. Ding, F. Lipparini, F. Egidi, J. Goings, B. Peng, A. Petrone, T. Henderson, D. Ranasinghe, V. G. Zakrzewski, J. Gao, N. Rega, G. Zheng, W. Liang, M. Hada, M. Ehara, K. Toyota, R. Fukuda, J. Hasegawa, M. Ishida, T. Nakajima, Y. Honda, O. Kitao, H. Nakai, T. Vreven, K. Throssell, J. A. Montgomery, Jr., J. E. Peralta, F. Ogliaro, M. J. Bearpark, J. J. Heyd, E. N. Brothers, K. N. Kudin, V. N. Staroverov, T. A. Keith, R. Kobayashi, J. Normand, K. Raghavachari, A. P. Rendell, J. C. Burant, S. S. Iyengar, J. Tomasi, M. Cossi, J. M. Millam, M. Klene, C. Adamo, R. Cammi, J. W. Ochterski, R. L. Martin, K. Morokuma, O. Farkas, J. B. Foresman, and D. J. Fox. Gaussian 16 Revision C.01. Technical report, Gaussian Inc. Wallingford CT, 2016.

M. L. Goldberg. *Pyrite oxidation in acid mine drainage systems: Oxygen isotope systematics of intermediate sulfoxyanions in sociopolitical context*. Undergraduate thesis, Harvard University, 2021.

J. Hayles, C. Gao, X. Cao, Y. Liu, and H. Bao. Theoretical calibration of the triple oxygen isotope thermometer. *Geochimica et Cosmochimica Acta*, 235:237–245, 2018.

J. D. Hemingway, H. Olson, A. V. Turchyn, E. T. Tipper, M. J. Bickle, and D. T. Johnston. Triple oxygen isotope insight into terrestrial pyrite oxidaiton. *Proceedings of the National Academy of Sciences*, 117:7650–7657, 2020.

J. Horita, D. R. Cole, and D. J. Wesolowski. The activity-composition relationship of oxygen and hydrogen isotopes in aqueous salt solutions: III. Vapor-liquid water equilibrium of NaCl solutions to 350°C. *Geochimica et Cosmochimica Acta*, 59:1139–1151, 1995.

J. Horita, K. Rozanski, and S. Cohen. Isotope effects in the evaporation of water: a status report of the Craig–Gordon model. *Isotopes in Environmental and Health Studies*, 44:23–49, 2008.

K. K. Irikura, R. D. Johnson III, and R. N. Kacker. Uncertainties in scaling factors for *ab initio* vibrational frequencies. *Journal of Physical Chemistry A*, 109:8430–8437, 2005.

K. K. Irikura, R. D. Johnson, R. Kacker, and R. Kessel. Uncertainties in scaling factors for *ab initio* vibrational zero-point energies. *Journal of Chemical Physics*, 130:114102, 2009.

R. D. Johnson III, editor. *NIST Computational Chemistry Comparison and Benchmark Database*. Number 101 in 21. National Institute of Standards and Technology, http://cccbdb.nist.gov/, 2020.

F. Johnston and L. McAmish. A study of the rates of sulfur production in acid thiosulfate solutions using S-35. *Journal of Colloid and Interface Science*, 42:112–119, 1973.

B. B. Jørgensen. A thiosulfate shunt in the sulfur cycle of marine sediments. *Science*, 249:152–154, 1990.

P. Kemeny, G. Lopez, N. Dalleska, M. Torres, A. Burke, M. Bhatt, A. J. West, J. Hartmann, and J. F. Adkins. Sulfate sulfur isotopes and major ion chemistry reveal that pyrite oxidation counteracts CO_2 drawdown from silicate weathering in the Langtang-Trisuli-Narayani River system, Nepal Himalaya. *Geochimica et Cosmochimica Acta*, 294:43–69, 2021.

R. A. Kendall, T. H. Dunning, Jr., and R. J. Harrison. Electron affinities of the first-row atoms revisited. Systematic basis sets and wave functions. *Journal of Chemical Physics*, 96:6796–6806, 1992.

B. A. Killingsworth, H. Bao, and I. E. Kohl. Assessing pyrite-derived sulfate in the Mississippi River with four years of sulfur and triple-oxygen isotope data. *Environmental Science & Technology*, 52:6126–6136, 2018.

I. Kohl and H. Bao. Triple-oxygen-isotope determination of molecular oxygen incorporation in sulfate produced during abiotic pyrite oxidation (pH = 2-11). *Geochimica et Cosmochimica Acta*, 75:1785–1798, 2011.

I. Kohl, R. Asatryan, and H. Bao. No oxygen isotope exchange between water and aps-sulfate at surface temperature: evidence from quantum chemical modeling and triple-oxygen isotope experiments. *Geochimica et Cosmochimica Acta*, 95:106–118, 2012.

C. Lee, W. Yang, and R. G. Parr. Development of the Colle-Salvetti correlation-energy formula into a functional of the electron density. *Physical Review B*, 37:785–789, 1988.

X. Li and Y. Liu. Equilibrium Se isotope fractionation parameters: a first-principles study. *Earth and Planetary Science Letters*, 304:113–120, 2011.

X. Li, H. Zhao, M. Tang, and Y. Liu. Theoretical prediction for several important equilibrium Ge isotope fractionation factors and geological implications. *Earth and Planetary Science Letters*, 287:1–11, 2009.

Q. Liu, J. A. Tossell, and Y. Liu. On the proper use of the Bigeleisen-Mayer equation and corrections to it in the calculation of isotopic fractionation equilibrium constants. *Geochimica et Cosmochimica Acta*, 74:6965–6983, 2010.

R. Lloyd. Oxygen isotope behavior in the sulfate-water system. *Journal of Geophysical Research*, 73:6099–6110, 1968.

B. Luz and E. Barkan. Net and gross oxygen production from O_2/Ar, $^{17}O/^{16}O$, and $^{18}O/^{16}O$ ratios. *Aquatic Microbial Ecology*, 56:133–145, 2009.

A. Masterson, M. J. Alperin, W. M. Berelson, and D. T. Johnston. Interpreting multiple sulfur isotope signals in modern anoxic sediments using a full diagenetic model (California-Mexico Margin: Alfonso Basin). *American Journal of Science*, 318:459–490, 2018.

A. J. Masterson, M. J. Alperin, G. L. Arnold, W. M. Berelson, B. B. Jørgensen, H. Røy, and D. T. Johnston. Un-

derstanding the isotopic composition of sedimentary sulfide: a multiple sulfur isotope diagenetic model for Aarhus Bay. *American Journal of Science*, accepted, 2021.

J. P. Merrick, D. Moran, and L. Radom. An evaluation of harmonic vibrational frequency scale factors. *Journal of Physical Chemistry A*, 111:11683–11700, 2007.

F. J. Millero, J. P. Hershey, G. Johnson, and J.-Z. Zhang. The solubility of SO_2 and the dissociation of H_2SO_3 in NaCl solutions. *Journal of Atmospheric Chemistry*, 8:377–389, 1989.

C. Møller and M. Plesset. Note on an approximation treatment for many-electron systems. *Physical Review*, 46: 618–622, 1934.

I. A. Müller, B. Brunner, C. Breuer, M. Coleman, and W. Bach. The oxygen isotope equilibrium fractionation between sulfite species and water. *Geochimica et Cosmochimica Acta*, 120:562–581, 2013a.

I. A. Müller, B. Brunner, and M. Coleman. Isotopic evidence of the pivotal role of sulfite oxidation in shaping the oxygen isotope signature of sulfate. *Chemical Geology*, 354:186–202, 2013b.

J. J. Novoa and C. Sosa. Evaluation of the density function approximation on the computation of hydrogen bond interactions. *Journal of Physical Chemistry*, 99:15837–15845, 1995.

W. A. Pryor and U. Tonellato. Nucleophilic displacement at sulfur III. the exchange of oxygen-18 between sodium thiosulfate-^{18}O and water. *Journal of the American Chemical Society*, 89:3379–3386, 1967.

O. Redlich. Eine allgemeine beziehung zwischen den schwingungsfrequenzen isotoper molekln. *Zeitschrift für Physikalische Chemie*, 28:371–382, 1935.

P. Richet, Y. Bottinga, and J. M. A review of hydrogen, carbon, nitrogen, oxygen, sulphur, and chlorine stable isotope fractionation among gaseous molecules. *Annual Reviews of Earth and Planetary Sciences*, 5:65–110, 1977.

J. D. Rimstidt and D. J. Vaughan. Pyrite oxidation: a state-of-the-art assessment of the reaction mechanism. *Geochimica et Cosmochimica Acta*, 67:873–880, 2003.

E. A. Schauble and E. D. Young. Mass dependence of equilibrium oxygen isotope fractionation in carbonate, nitrate, oxide, perchlorate, phosphate, silicate, and sulfate minerals. *Reviews in Mineralogy & Geochemistry*, 86:137–178, 2021.

M. A. Schoonen, A. D. Harrington, R. Laffers, and D. R. Strongin. Role of hydrogen proxide and hydroxyl radical in pyrite oxidation by molecular oxygen. *Geochimica et Cosmochimica Acta*, 74:4971–1987, 2010.

A. P. Scott and L. Radom. Harmonic vibrational frequencies: an evaluation of hartree-fock, møller-plesset, quadratic configuration interaction, density functional theory, and semiempirical scale factors. *Journal of Physical Chemistry*, 100:16502–16513, 1996.

G. E. Scuseria, C. L. Janssen, and H. F. Schaefer. An efficient reformulation of the closed-shell coupled cluster single and double excitation (CCSD) equations. *Journal of Chemical Physics*, 89:7382–7387, 1988.

Z. D. Sharp and J. A. Wostbrock. Standardizations for the triple oxygen isotope system: waters, silicates, carbonates, air, and sulfates. *Reviews in Mineralogy & Geochemistry*, 86:179–196, 2021.

D. A. Teagle, J. C. Alt, and A. N. Halliday. Tracing the chemical evolution of fluids during hydrothermal recharge:

constraints from anhydrite recovered in ODP Hole 504B. *Earth and Planetary Science Letters*, 155:167–182, 1998.

M. H. Thiemens and M. Lin. Discoveries of mass independent isotope effects in the solar system: past, present, and future. *Reviews in Mineralogy & Geochemistry*, 86:35–95, 2021.

A. V. Turchyn, E. T. Tipper, A. Galy, J.-K. Lo, and M. J. Bickle. Isotope evidence for secondary sulfide precipitation along the Marsiyandi River, Nepal, Himalayas. *Earth and Planetary Science Letters*, 374:36–46, 2013.

H. C. Urey. The thermodynamic properties of isotopic substances. *Journal of the Chemical Society*, pages 562–581, 1947.

A. Vairavamurthy, B. Manowitz, G. Luther III, and Y. Jeon. Oxidation state of sulfur in thiosulfate and implications for anaerobic energy metabolism. *Geochimica et Cosmochimica Acta*, 57:1619–1623, 1993.

A. Waldeck, B. Cowie, E. Bertran, B. Wing, I. Halevy, and D. Johnston. Deciphering the atmospheric signal in marine sulfate oxygen isotope composition. *Earth and Planetary Science Letters*, 522:12–19, 2019.

S. D. Wankel, A. S. Bradley, D. L. Eldridge, and D. T. Johnston. Determination and application of the equilibrium oxygen isotope effect between water and sulfite. *Geochimica et Cosmochimica Acta*, 125:694–711, 2014.

C. Weinzierl, M. Regelous, K. Haase, W. Bach, F. Böhm, D. Garbe-Schönberg, Y. Sun, M. Joachimski, and S. Krumm. Cretaceous seawater and hydrothermal fluid compositions recorded in abiogenic carbonates from the Troodos Ophiolite, Cyprus. *Chemical Geology*, 494:43–55, 2018.

M. A. Williamson and J. D. Rimstidt. The kinetics and electrochemical rate-determining step of aqueous pyrite oxidation. *Geochimica et Cosmochimica Acta*, 58:5443–5454, 1994.

E. B. Wilson, J. G. Decius, and P. G. Cross. *Molecular Vibrations*, volume 23. American Journal of Physics, 1955.

B. A. Wing and I. Halevy. Intracellular metabolite levels shape sulfur isotope fractionation during microbial sulfate reduction. *Proceedings of the National Academy of Sciences*, 111:18116–18125, 2014.

Y. Xu and M. A. Schoonen. The stability of thiosulfate in the presence of pyrite in low-temperature aqueous solutions. *Geochimica et Cosmochimica Acta*, 59:4605–4622, 1995.

Y. Xu, M. Schoonen, D. Nordstrom, K. Cunningham, and J. Ball. Sulfur geochemistry of hydrothermal waters in Yellowstone National Park: I. the origin of thiosulfate in hot spring waters. *Geochimica et Cosmochimica Acta*, 62:3729–3743, 1998.

L. Y. Yeung and J. A. Hayles. Climbing to the top of Mount Fuji: uniting theory and observations of oxygen triple isotope systematics. *Reviews in Mineralogy & Geochemistry*, 86:97–137, 2021.

E. D. Young, A. Galy, and H. Nagahara. Kinetic and equilibrium mass-dependent isotope fractionation laws in nature and their geochemical and cosmochemical significance. *Geochimica et Cosmochimica Acta*, 66:1095–1104, 2002.

R. E. Zeebe. A new value for the stable oxygen isotope fractionation between dissolved sulfate ion and water. *Geochimica et Cosmochimica Acta*, 74:818–828, 2010.

Y. Zhang and Y. Liu. The theory of equilibrium isotope fractionations for gaseous molecules under super-cold conditions. *Geochimica et Cosmochimica Acta*, 238:123–149, 2018.

7. Supplemental Table Captions

Table S.1: Bond lengths and angles for all gaseous species calculated using all computational methods used in this study [B3LYP/6-31+G(d,p), CCSD/aug-cc-pVTZ, and MP2/aug-cc-pVTZ].

Table S.2: Resulting harmonic frequencies (ω; cm^{-1}) and zero-point energies (harmonic and anharmonic ZPE; cm^{-1}) for all gaseous species calculated using all computational methods used in this study [B3LYP/6-31+G(d,p), CCSD/aug-cc-pVTZ, and MP2/aug-cc-pVTZ].

Table S.3: Bond lengths and angles for all aqueous sulfoxyanion species calculated using the B3LYP/6-31+G(d,p) computational method. For comparison, results from Eldridge et al. (2016) are also included.

Table S.4: Resulting harmonic frequencies (ω; cm^{-1}) and harmonic zero-point energies (ZPE; cm^{-1}) for all aqueous sulfoxyanion species and dissolved $O_{2(aq.)}$ calculated using the B3LYP/6-31+G(d,p) computational method.

Table S.5: Compilation of experimentally determined ${}^{18}\alpha_{anion/H_2O(liq.)}(T)$ values for sulfate, sulfite, and thiosulfate species. Data from: Lloyd (1968); Chiba et al. (1981); Müller et al. (2013a); Wankel et al. (2014); Goldberg (2021).

8. Supplemental Figures

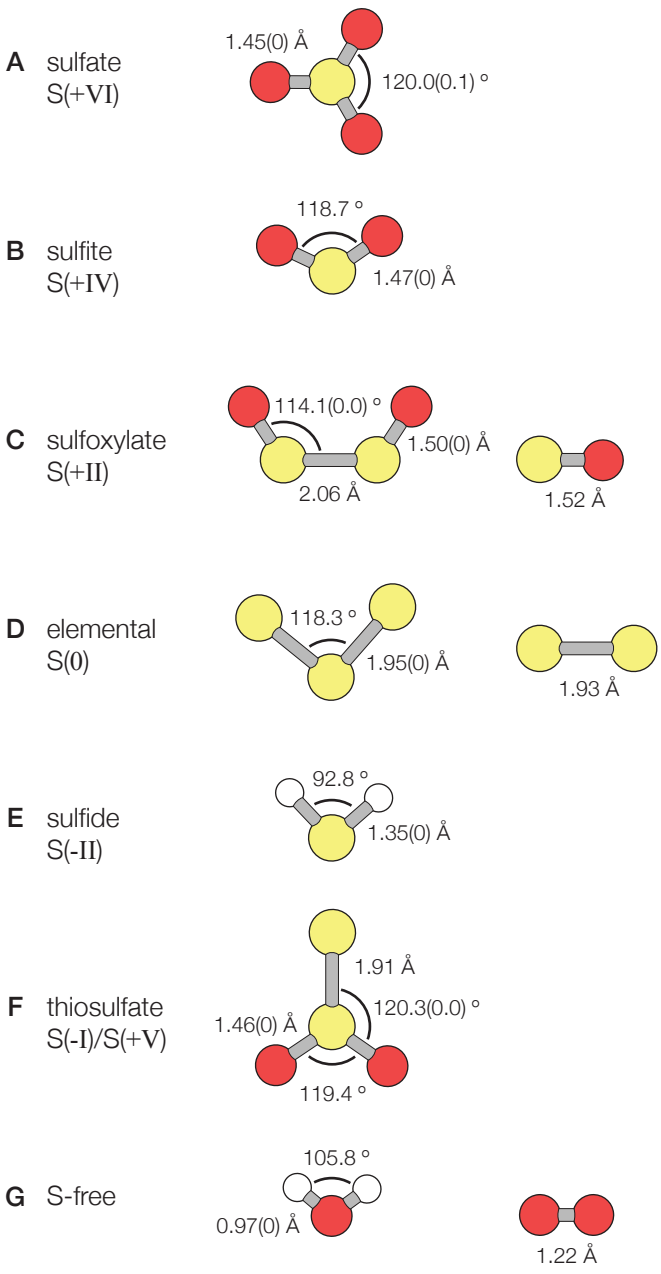

Figure S.1: **Ball-and-stick representation of each *in vacuo* species.** Species are separated by sulfur redox state: (**A**) sulfate species, S(+VI): SO_3; (**B**) sulfite species, S(+IV): SO_2; (**C**) sulfoxylate species, S(+II): S_2O_2 and SO; (**D**) elemental sulfur species, S(0): S_2 and S_3; (**E**) sulfide species, S(-II): H_2S; (**F**) thiosulfate species, mixed valence [S(-I) sulfanyl and S(+V) sulfonate]: $(S)SO_2$; and (**G**) S-free species: H_2O and O_2. Reported bond lengths and angles refer to those calculated using the B3LYP/6-31+G(d,p) method (corresponding CCSD/aug-cc-pVTZ and MP2/aug-cc-pVTZ results are additionally reported in Table S1).

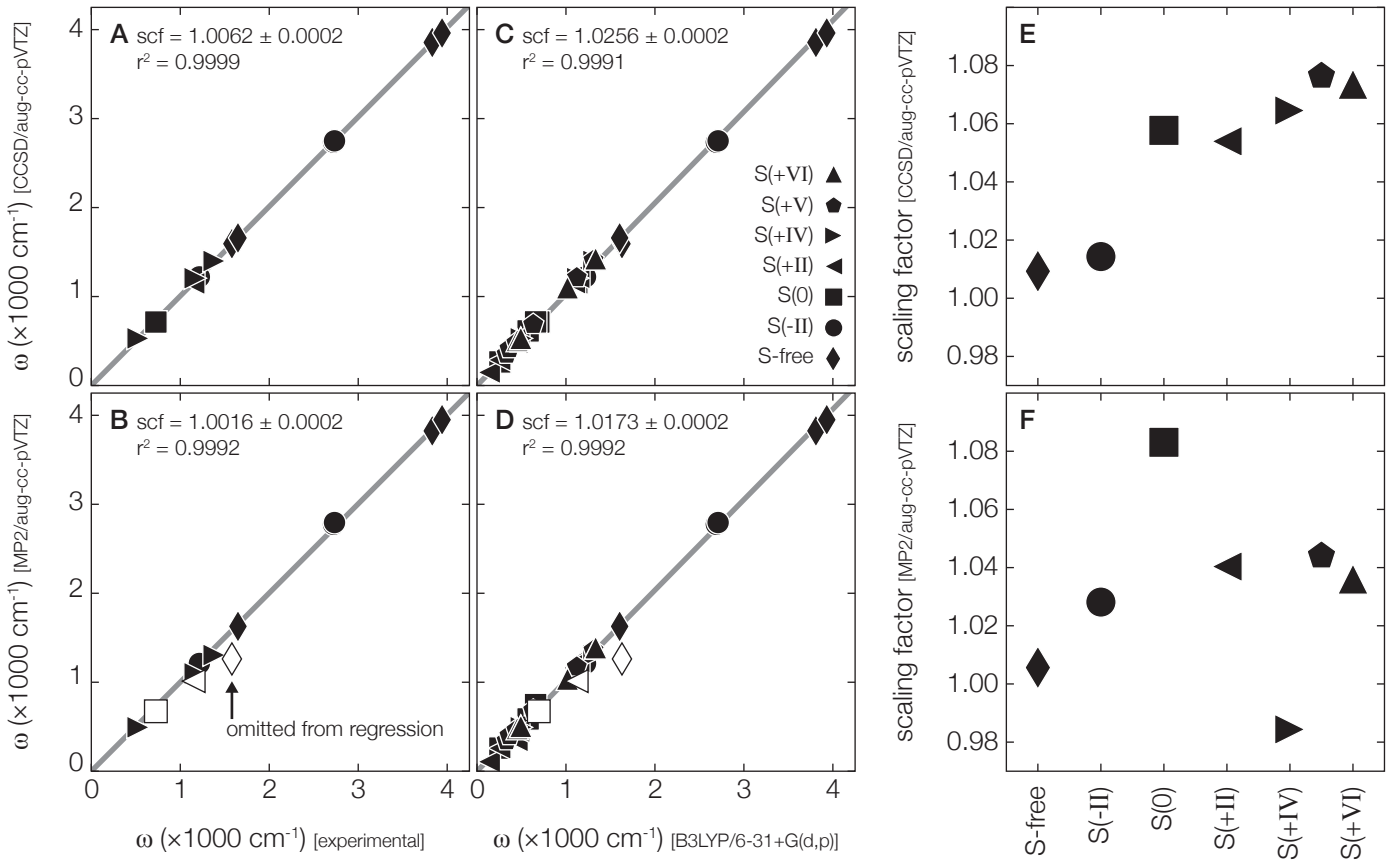

Figure S.2: **Harmonic frequency scaling factors.** ω values for all gaseous species of interest [H_2O, O_2, H_2S, S_2, S_3, SO, S_2O_2, SO_2, (S)SO_2, and SO_3] calculated using (**top**) CCSD/aug-cc-pVTZ and (**bottom**) MP2/aug-cc-pVTZ methods plotted as a function of (**A, B**) experimentally measured ω values (H_2O, O_2, H_2S, S_2, SO, and SO_2 only; Johnson III, 2020) and (**C, D**) ω values calculated using the B3LYP/6-31+G(d,p) method. All-compound-average scaling factors are calculated using using orthogonal distance regression (ODR; gray lines), which allows for uncertainty in both x and y variables, and are reported as $\mu \pm 1\sigma$. Redox-state-specific ODR scaling factors for (**E**) CCSD/aug-cc-pVTZ and (**F**) MP2/aug-cc-pVTZ ω values as a function of B3LYP/6-31+G(d,p) ω values are also shown; uncertainty is smaller than markers for all points. Diatomic molecules have been excluded from all regressions containing MP2/aug-cc-pVTZ ω values (white markers) since these are observed to deviate significantly from experimental results. Marker shapes refer to redox state of oxygen-bound sulfur for each species: diamonds = sulfur-free; circles = S(-II); squares = S(0); left-pointing triangles = S(+II), right-pointing triangles = S(+IV); pentagons = S(+V), upward-pointing triangles = S(+VI).

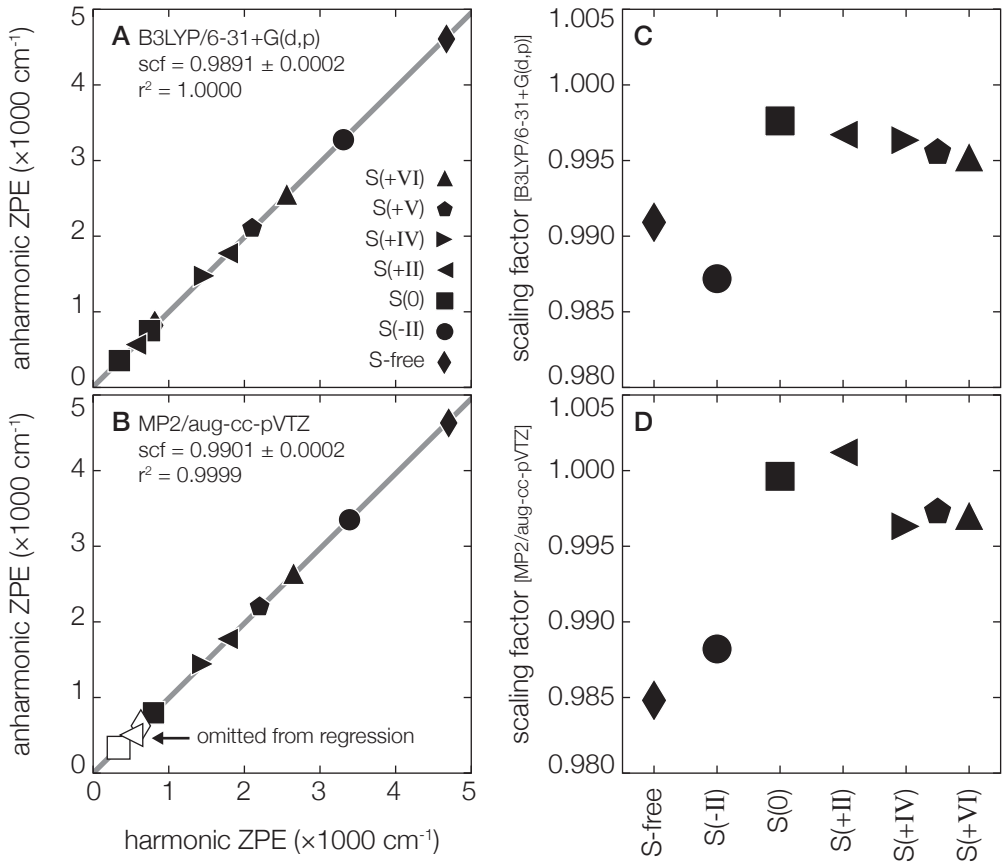

Figure S.3: **Zero-point energy scaling factors.** Anharmonic zero-point energy (ZPE) values for all gaseous species of interest [H_2O, O_2, H_2S, S_2, S_3, SO, S_2O_2, SO_2, (S)SO_2, and SO_3] calculated using (**A**) B3LYP/6-31+G(d,p) and (**B**) MP2/aug-cc-pVTZ methods plotted as a function of their corresponding harmonic zero-point energy values. All-compound-average scaling factors are calculated using using orthogonal distance regression (ODR; gray lines), which allows for uncertainty in both x and y variables, and are reported as $\mu \pm 1\sigma$. Redox-state-specific ODR scaling factors for (**C**) B3LYP/6-31+G(d,p) and (**D**) MP2/aug-cc-pVTZ anharmonic ZPE as a function of corresponding harmonic ZPE are also shown; uncertainty is smaller than markers for all points. Diatomic molecules have been excluded from all regressions containing MP2/aug-cc-pVTZ ZPE values (white markers) since ω values for these compounds are observed to deviate significantly from experimental results. Marker shapes refer to redox state of oxygen-bound sulfur for each species: diamonds = sulfur-free; circles = S(-II); squares = S(0); left-pointing triangles = S(+II), right-pointing triangles = S(+IV); pentagons = S(+V), upward-pointing triangles = S(+VI).

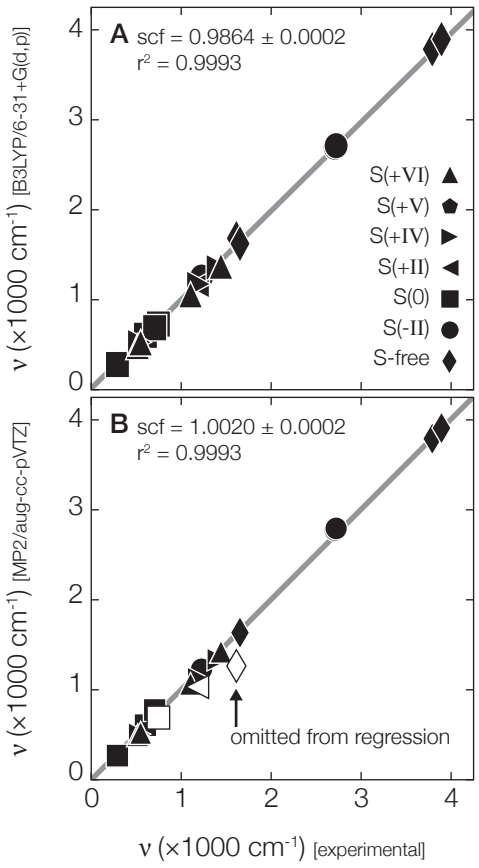

Figure S.4: **Fundamental frequency scaling factors.** Experimental vs. calculated ν values for all gaseous species of interest for which experimental results exist (H_2O, O_2, H_2S, S_2, S_3 SO, SO_2, and SO_3; Johnson III, 2020) calculated using (**A**) B3LYP/6-31+G(d,p) and (**B**) MP2/aug-cc-pVTZ methods. All-compound-average scaling factors are calculated using using orthogonal distance regression (ODR; gray lines), which allows for uncertainty in both x and y variables, and are reported as $\mu \pm 1\sigma$. Diatomic molecules have been excluded from all regressions containing MP2/aug-cc-pVTZ ZPE values (white markers) since ν values for these compounds are observed to deviate significantly from experimental results. Marker shapes refer to redox state of oxygen-bound sulfur for each species: diamonds = sulfur-free; circles = S(-II); squares = S(0); left-pointing triangles = S(+II), right-pointing triangles = S(+IV); pentagons = S(+V), upward-pointing triangles = S(+VI).

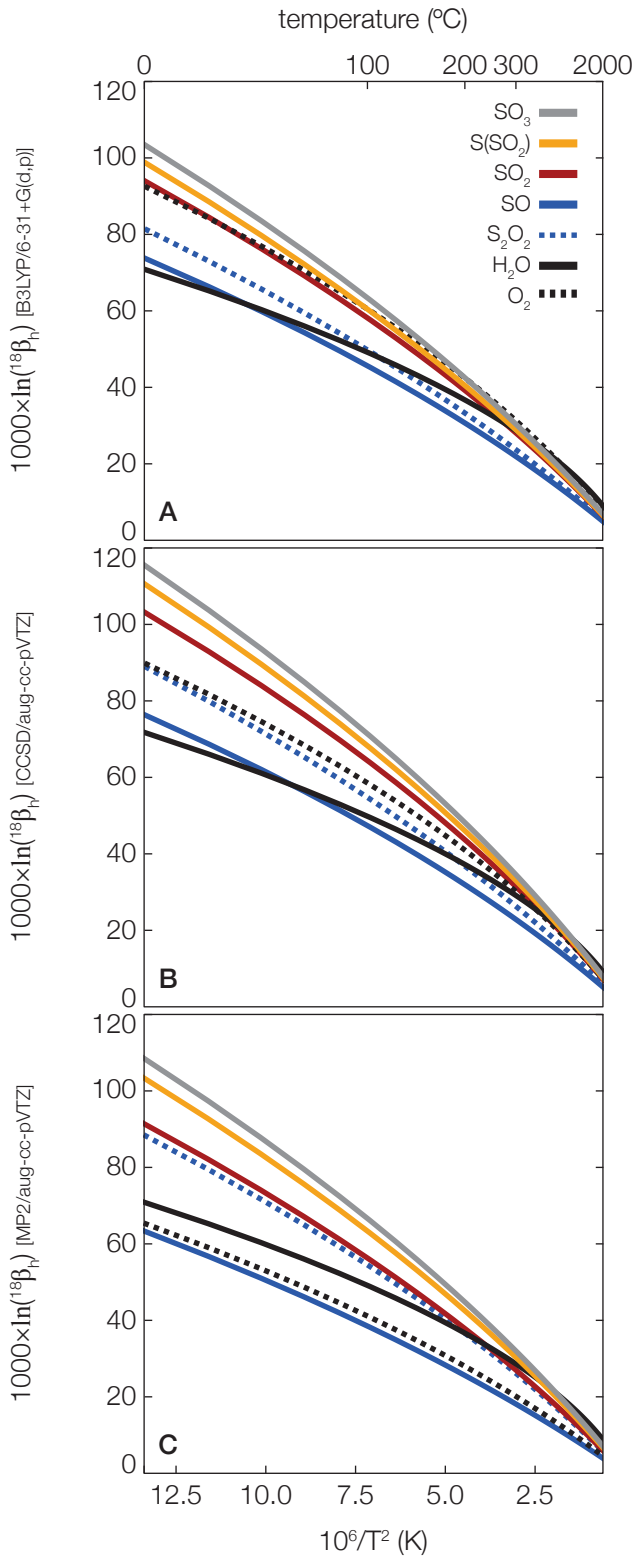

Figure S.5: **Harmonic $^{18}\beta(T)$ results for gaseous species.** Harmonic partition function ratios [$^{18}\beta_h(T)$] plotted as a function temperature for all oxygen-containing gaseous species of interest using various methods and basis sets: (**A**) B3LYP/6-61+G(d,p), unscaled ω values; (**B**) CCSD/aug-cc-pVTZ; (**C**) MP2/aug-cc-pVTZ. Line styles refer to each species: solid black = H_2O; dotted black = O_2; solid blue = SO; dotted blue = S_2O_2; red = SO_2, yellow = (S)SO_2, gray = SO_3.

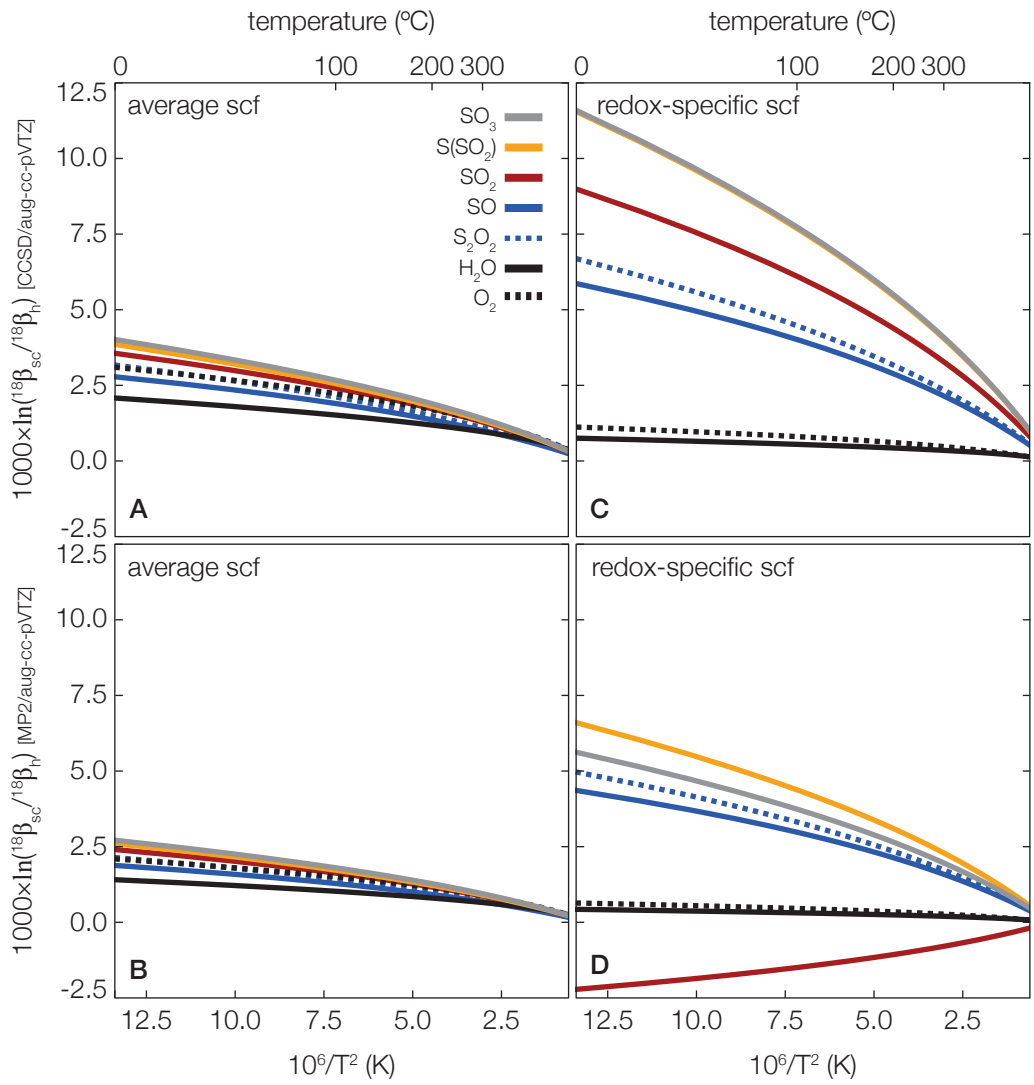

Figure S.6: **Scaled harmonic $^{18}\beta(T)$ results for gaseous species.** Scaling offsets from B3LYP/6-31+G(d,p) $^{18}\beta_{\mathrm{h}}(T)$ values plotted as a function temperature for all oxygen-containing gaseous species. Offsets are plotted as $1000 \times \ln\left[{}^{18}\beta_{\mathrm{h}}(T)/{}^{18}\beta_{\mathrm{sc}}(T)\right]$ where $^{18}\beta_{\mathrm{sc}}(T)$ refers to the $^{18}\beta_{\mathrm{h}}(T)$ value calculated using B3LYP/6-31+G(d,p) ω values multiplied by scaling factors for: (**A**) CCSD/aug-cc-pVTZ, all-compound-average; (**B**) MP2/aug-cc-pVTZ, all-compound-average; (**C**) CCSD/aug-cc-pVTZ, redox-state-specific; (**D**) MP2/aug-cc-pVTZ, redox-state-specific. Line styles refer to each species: solid black = H_2O; dotted black = O_2; solid blue = SO; dotted blue = S_2O_2; red = SO_2, yellow = (S)SO_2, gray = SO_3.

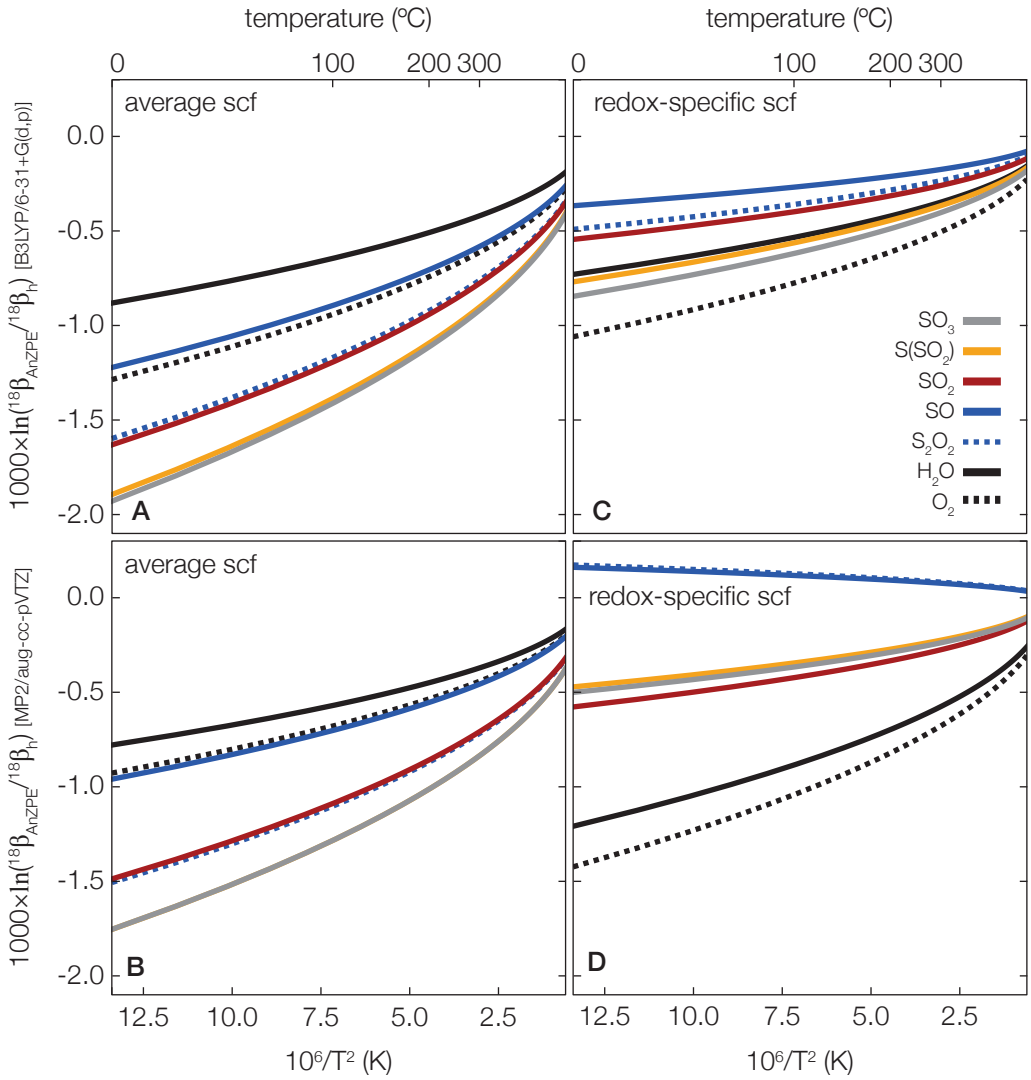

Figure S.7: **Anharmonic ZPE $^{18}\beta(T)$ results for gaseous species.** Anharmonic zero-point energy (ZPE) scaling offsets from corresponding harmonic $^{18}\beta_{\mathrm{h}}(T)$ values plotted as a function temperature for all oxygen-containing gaseous species. Offsets are plotted as $1000 \times \ln\left[{}^{18}\beta_{\mathrm{AnZPE}}(T)/{}^{18}\beta_{\mathrm{h}}(T)\right]$ where $^{18}\beta_{\mathrm{AnZPE}}(T)$ refers to the $^{18}\beta_{\mathrm{h}}(T)$ value calculated using harmonic ZPE values multiplied by scaling factors for: (**A**) B3LYP/6-31+G(d,p), all-compound-average ZPE scaling; (**B**) MP2/aug-cc-pVTZ, all-compound-average ZPE scaling; (**C**) B3LYP/6-31+G(d,p), redox-state-specific ZPE scaling; (**D**) MP2/aug-cc-pVTZ, redox-state-specific ZPE scaling. Line styles refer to each species: solid black = H_2O; dotted black = O_2; solid blue = SO; dotted blue = S_2O_2; red = SO_2, yellow = (S)SO_2, gray = SO_3.

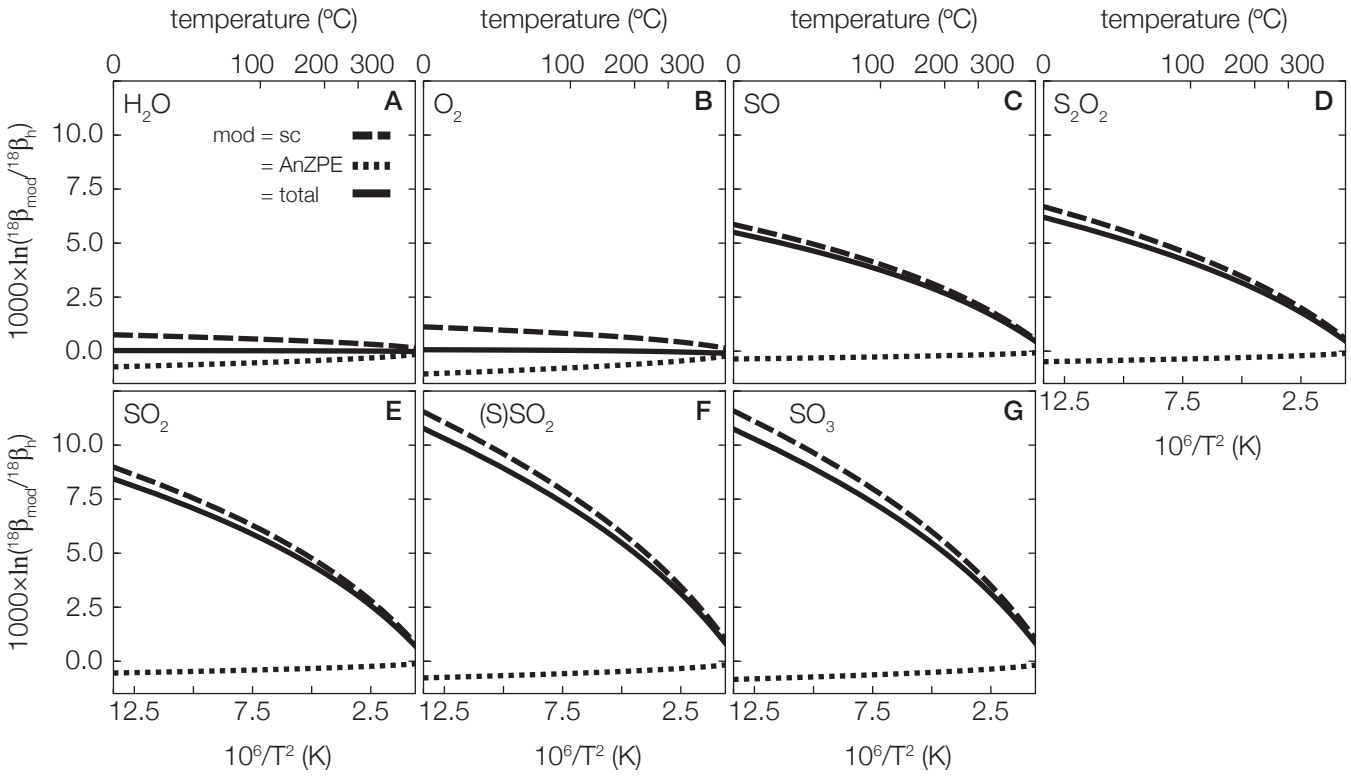

Figure S.8: **Final $^{18}\beta(T)$ corrections used throughout this study.** Total scaling factor offsets for (**A**) H_2O, (**B**) O_2, (**C**) SO, (**D**) S_2O_2, (**E**) SO_2, (**F**) (S)SO_2, and (**G**) SO_3 as a function of temperature. For each panel, $^{18}\beta_{sc}(T)$ is calculated using the redox-state-specific scaling factor for B3LYP/6-31+G(d,p) scaled to CCSD/aug-cc-pVTZ ω values, $^{18}\beta_{AnZPE}(T)$ is calculated using the redox-state-specific AnZPE scaling factor for B3LYP/6-31+G(d,p), and $^{18}\beta_{sc,AnZPE}(T)$ represents the combined effect of $^{18}\beta_{sc}(T)$ and $^{18}\beta_{AnZPE}(T)$. Resulting $^{18}\beta_{sc,AnZPE}(T)$ scaling is similarly applied to all solvated species throughout this study.

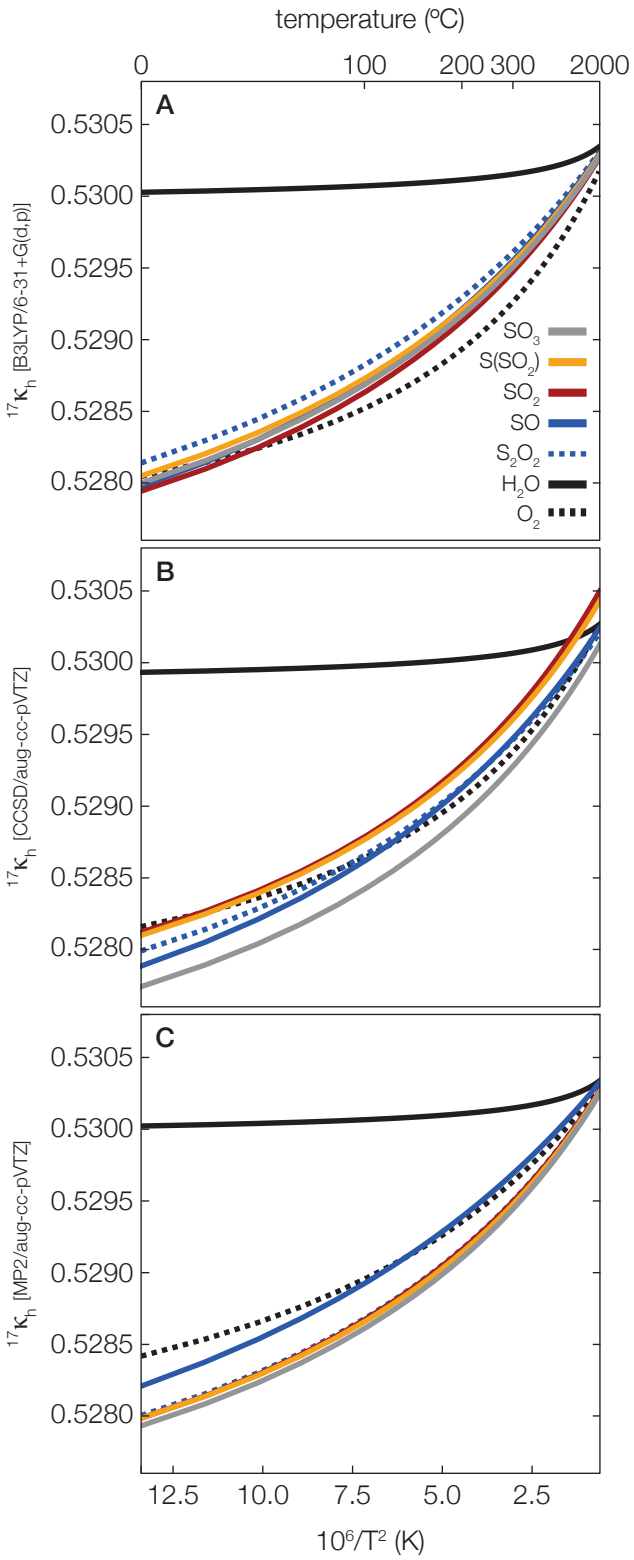

Figure S.9: **Harmonic $^{17}\kappa(T)$ results for gaseous species.** Harmonic triple-isotope partition function ratios ($^{17}\kappa_h(T)$) plotted as a function temperature for all oxygen-containing gaseous species using various methods and basis sets: (**A**) B3LYP/6-61+G(d,p), unscaled ω values; (**B**) CCSD/aug-cc-pVTZ; (**C**) MP2/aug-cc-pVTZ. Line styles refer to each species: solid black = H_2O; dotted black = O_2; solid blue = SO; dotted blue = S_2O_2; red = SO_2, yellow = (S)SO_2, gray = SO_3.

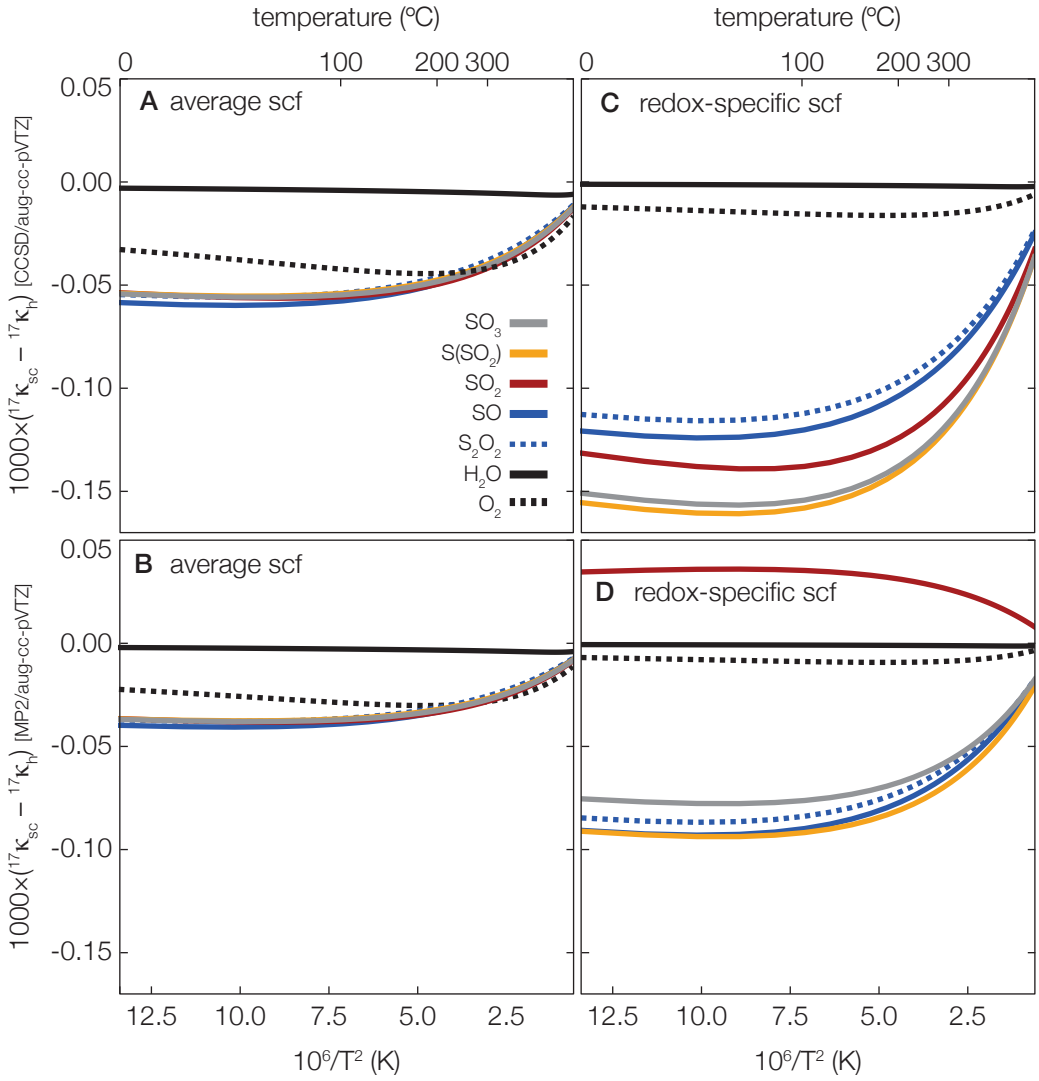

Figure S.10: **Scaled harmonic $^{17}\kappa(T)$ results for gaseous species.** Scaling offsets from B3LYP/6-31+G(d,p) $^{17}\kappa_h(T)$ values plotted as a function temperature for all oxygen-containing gaseous species. Offsets are plotted as $1000 \times \ln\left[{}^{17}\kappa_{sc}(T) - {}^{17}\kappa_h(T)\right]$ where $^{17}\kappa_{sc}(T)$ refers to the $^{17}\kappa_h(T)$ value calculated using B3LYP/6-31+G(d,p) ω values multiplied by scaling factors for: (**A**) CCSD/aug-cc-pVTZ, all-compound-average; (**B**) MP2/aug-cc-pVTZ, all-compound-average; (**C**) CCSD/aug-cc-pVTZ, redox-state-specific; (**D**) MP2/aug-cc-pVTZ, redox-state-specific. Line styles refer to each species: solid black = H_2O; dotted black = O_2; solid blue = SO; dotted blue = S_2O_2; red = SO_2, yellow = (S)SO_2, gray = SO_3.

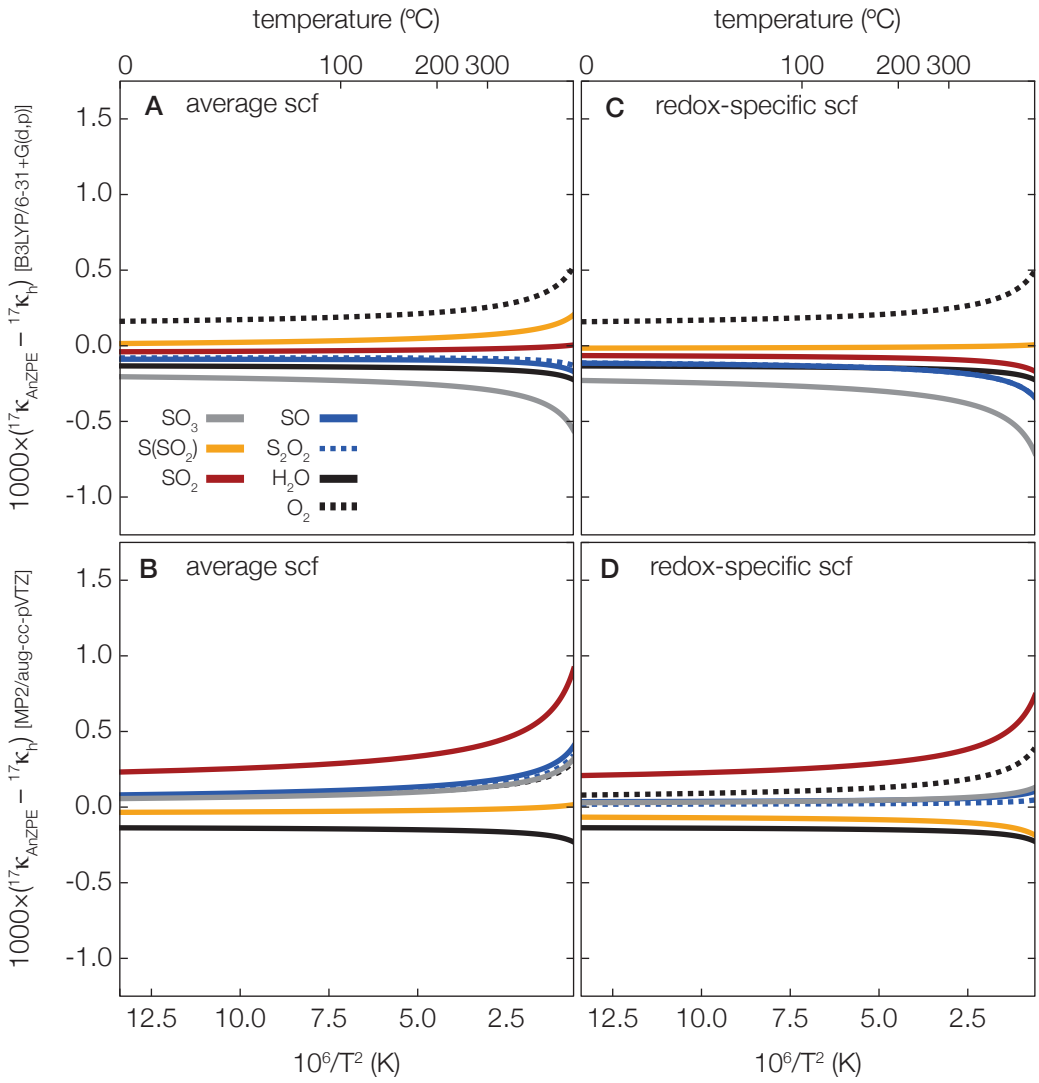

Figure S.11: **Anharmonic ZPE $^{17}\kappa(T)$ results for gaseous species.** Anharmonic ZPE scaling offsets from corresponding harmonic $^{17}\kappa_h(T)$ values plotted as a function temperature for all oxygen-containing gaseous species. Offsets are plotted as $1000 \times \left[{}^{17}\kappa_{AnZPE}(T) - {}^{17}\kappa_h(T)\right]$ where $^{17}\kappa_{AnZPE}(T)$ refers to the $^{17}\kappa_h(T)$ value calculated using harmonic ZPE values multiplied by scaling factors for: (**A**) B3LYP/6-31+G(d,p), all-compound-average ZPE scaling; (**B**) MP2/aug-cc-pVTZ, all-compound-average ZPE scaling; (**C**) B3LYP/6-31+G(d,p), redox-state-specific ZPE scaling; (**D**) MP2/aug-cc-pVTZ, redox-state-specific ZPE scaling. Line styles refer to each species: solid black = H_2O; dotted black = O_2; solid blue = SO; dotted blue = S_2O_2; red = SO_2, yellow = (S)SO_2, gray = SO_3. Note that offsets increase with increasing temperature—as is observed here for most compounds—if $^{17}\kappa_{AnhC} \neq 0.5305$, where $^{17}\kappa_{AnhC} = \ln(^{18}\beta_{AnhC})/\ln(^{17}\beta_{AnhC})$ and $^{*}\beta_{AnhC}$ refers only to the contribution due to anharmonic ZPE correction (c.f., Cao and Liu, 2011, their Eq. 12)

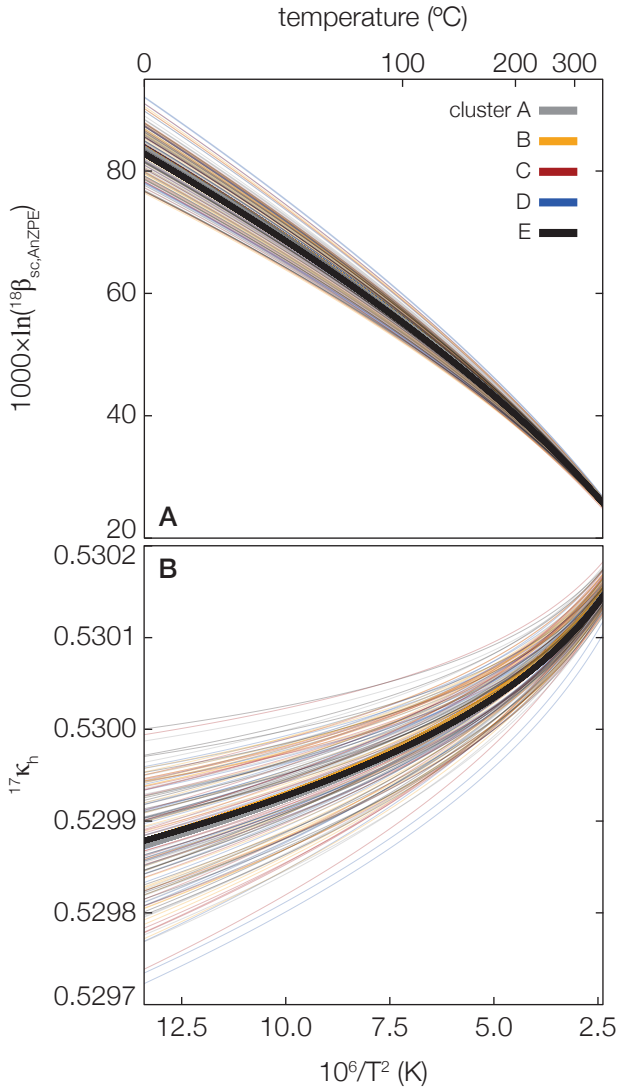

Figure S.12: **Theoretically derived water droplet $^{18}\beta(T)$ and $^{17}\kappa(T)$ results.** (**A**) $^{18}\beta_{\mathrm{sc,AnZPE}}(T)$ and (**B**) $^{17}\kappa_{\mathrm{h}}(T)$ values plotted as a function of temperature. Each thin line represents results for isotopically substituting a single water oxygen atom (n = 30 per cluster); thick lines represent cluster-averages (all are shown but only cluster E average is visible; others plot directly below the cluster E line). Results for each cluster (n = 5) are plotted as different colored lines.

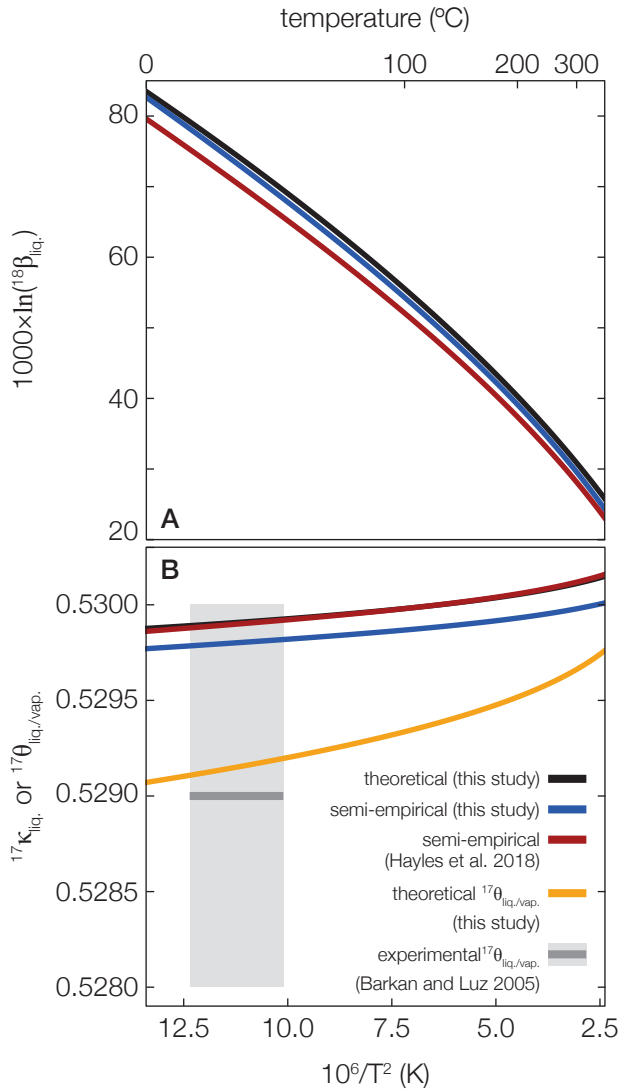

Figure S.13: **Comparison between theoretical and semi-empirical liquid water $^{18}\beta(T)$ and $^{17}\kappa(T)$ results.** (**A**) $^{18}\beta(T)$ and (**A**) $^{17}\kappa(T)$ values plotted as a function of temperature showing: pure theoretical results, this study (black); semi empirical results, this study following the method of Hayles et al. (2018) using experimental data from Horita et al. (2008) (blue); and semi-empirical results from Hayles et al. (2018) using the B3LYP/6-311+G(2df,p) method (red). All $^{18}\beta(T)$ results from this study include scaling and AnZPE corrections [i.e., $^{18}\beta_{sc,AnZPE}(T)$] whereas all $^{17}\kappa(T)$ results represent the harmonic approximation [i.e., $^{17}\kappa_h(T)$]. Also shown in panel (**B**) is the theoretically (yellow) and experimentally (gray, Barkan and Luz, 2005) determined $^{17}\theta$ value for $H_2O_{(liq.)}/H_2O_{(vap.)}$ fractionation, including experimental uncertainty (gray shaded region).